

1 **Methane intensity and emissions across major oil and gas basins**  
2 **and individual jurisdictions using MethaneSAT observations**

3 James P. Williams<sup>1,2</sup>, Joshua Benmergui<sup>1,2,3</sup>, Marvin Knapp<sup>1,2,3</sup>, Mark Omara<sup>1,2</sup>, Anthony  
4 Himmelberger<sup>1,2</sup>, Ethan Kyzivat<sup>3</sup>, Kaiya Weatherby<sup>1,2</sup>, Ben Lyke<sup>1,2</sup>, Jack Warren<sup>1,2</sup>, Katlyn  
5 MacKay<sup>1,2</sup>, Sasha Ayvazov<sup>2</sup>, Marcus Russi<sup>2</sup>, Nicholas LoFaso<sup>2</sup>, Tom Melendez<sup>2</sup>, Christopher C.  
6 Miller<sup>1,2,3</sup>, Sebastien Roche<sup>1,2,3</sup>, Maryann Sargent<sup>3</sup>, Jonathan Franklin<sup>3</sup>, Maya Nasr<sup>3</sup>, Zhan  
7 Zhang<sup>3</sup>, David J. Miller<sup>3</sup>, Bingkun Luo<sup>3</sup>, Luis Guanter<sup>1,4</sup>, Steven P. Hamburg<sup>1,2</sup>, Steven C.  
8 Wofsy<sup>3</sup>, Ritesh Gautam<sup>1,2</sup>

9 <sup>1</sup>Environmental Defense Fund, New York, NY, USA 10010

10 <sup>2</sup>MethaneSAT, LLC, Austin, TX, USA 78701

11 <sup>3</sup>Harvard John A. Paulson School of Engineering and Applied Sciences, Harvard University, Cambridge,  
12 MA, USA 02138

13 <sup>4</sup>Research Institute of Water and Environmental Engineering (IIAMA), Universitat Politècnica de  
14 València, Valencia, Spain

15  
16

17 *Correspondence to:* James P. Williams ([jamwilliams@edf.org](mailto:jamwilliams@edf.org)), Ritesh Gautam ([rgautam@edf.org](mailto:rgautam@edf.org))

18

19 **Abstract.** Mitigating anthropogenic methane emissions is widely recognized as an effective strategy to reduce near-  
20 term climate warming. Here, we use satellite observations from MethaneSAT (2024–2025) to characterize methane  
21 emissions from ~~six oil and gas producing regions as a demonstration of MethaneSAT data capabilities~~. MethaneSAT  
22 ~~was designed~~ to address a gap in quantitative data of ~~spatially-resolved~~ emissions, ~~by providing high-resolution area~~  
23 emissions (~4 × 4 km) with a wide-swath (220–440 km). The native pixel resolution of MethaneSAT is ~110 × 400  
24 m (at nadir) at which the column-averaged dry-air mole fraction of methane is retrieved before atmospheric  
25 inversion-based methane emissions data are produced. We analyze emissions data across six oil and gas producing  
26 regions: the Permian (USA), San Joaquin (USA), Eagle Ford (USA/Mexico), Amu Darya (Turkmenistan and  
27 Uzbekistan), and the Zagros Foldbelt (Iran/Iraq). Regional oil and gas emissions span more than an order of  
28 magnitude, ranging from 408 t h<sup>-1</sup> (95% c.i.: 303–516 t h<sup>-1</sup>) for the Permian basin to 30 t h<sup>-1</sup> (95% c.i.: 20–41 t h<sup>-1</sup>)  
29 in the San Joaquin basin. Methane intensities also vary substantially ~~by~~ more than an order of magnitude in both  
30 ~~gas-production-normalized and energy-normalized~~ metrics. These differences reflect diverse factors, including oil  
31 versus gas production, infrastructure age, lower-producing wells, ~~and emission mitigation controls~~. Across  
32 individual jurisdictions, including counties/districts, we find consistent underestimation by gridded EPA-GHGI and  
33 EDGAR bottom-up inventories relative to MethaneSAT-derived emissions. Overall, MethaneSAT data provide  
34 basin-wide and sub-regional insights into methane emissions and intensities, offering critical scientific and policy-  
35 relevant information to support targeted emission quantification and mitigation strategies.

36

Deleted: Harvard University, Cambridge, MA, USA 02138

Deleted: major oil and gas basins worldwide

Deleted: addresses a critical gap in access

Deleted: measurements

Deleted: spatially distributed

Deleted: .3

Deleted: .1

Deleted: across basins and sub-basins, with

Deleted: production-normalized and energy-normalized

Deleted: and presence or absence of emission mitigation practices

48

## 49 1 Introduction

50 Methane is a potent greenhouse gas has been identified as a crucial target for emissions reduction to meet near-term  
 51 climate change goals (Saunois et al., 2025). Due to the potency of methane as a greenhouse gas, more than 150  
 52 countries have pledged to reduce methane emissions as part of the Global Methane Pledge which was signed in  
 53 2021, with new actions introduced in the 29<sup>th</sup> United Nations Climate Change Conference in Azerbaijan held in  
 54 2024. Fortunately, several sectors responsible for significant portions of the anthropogenic methane budget offer  
 55 attainable mitigation pathways with reductions being achievable with existing technology and/or updated industry  
 56 practices (Nisbet et al., 2020). A crucial component of reducing methane emissions is the ability to detect, quantify,  
 57 and locate methane emissions over time, which in turn informs effective mitigation strategies. Bottom-up  
 58 inventories, such as the gridded Environmental Protection Agency Greenhouse Gas Inventory (EPA-GHGI)  
 59 (Maasakkers et al., 2023) and the Emissions Database for Global Atmospheric Research (EDGAR) (Crippa et al.,  
 60 2024), provide spatially explicit estimates used to track progress, but are limited by uncertainties in emission factors  
 61 and activity data (Jacob et al., 2022). Satellite-based measurements are used to inform bottom-up estimates and  
 62 highlight discrepancies, effectively improving knowledge on the location, magnitude, and sectors responsible for  
 63 methane emissions, and have rapidly expanded in recent years. Over a dozen methane sensing satellite platforms are  
 64 currently in orbit, either as single “stand-alone” instruments (e.g., TROPOMI) (Veeffkind et al., 2012) or as  
 65 constellations that increase revisit frequency, (e.g., GHGSat) (Jervis et al., 2021). Broadly, methane sensing  
 66 satellites are categorized as either point source imagers or area flux mappers (Jacob et al., 2022). Point source  
 67 imagers, including GHGSat (Jervis et al., 2021) and Carbon Mapper Planet Tanager (Duren et al., 2025), provide fine  
 68 spatial resolution observations (~25 – 30 m) that detect and quantify methane point sources at fine spatial resolutions  
 69 provided that the emission rate is above the detection threshold of the instrument, which in turn can be used to  
 70 determine the facility linked to the emissions (Warren et al., 2025). In contrast, area flux mappers such as  
 71 TROPOMI quantify methane emissions at regional or global scales using coarser-resolution observations combined  
 72 with inverse modelling frameworks and prior inventories to infer spatial allocation of emissions and sectoral  
 73 contributions (Lu et al., 2022; Nesser et al., 2024; Shen et al., 2022). Area flux mappers provide basin-scale  
 74 emission estimates at coarse spatial resolution, while point-source imagers offer fine spatial detail but are primarily  
 75 sensitive to the largest emitters, leaving a gap in the ability to resolve the full distribution of emissions at high  
 76 resolution across basin-scale domains.

77 MethaneSAT, which operated between March 2024 and June 2025, was designed to provide methane observations at  
 78 intermediate spatial scales, with a native sampling resolution of  $\sim 100 \times 400 \text{ m}^2$  and wide swath coverage ( $\sim 220 -$   
 79  $440 \text{ km}$ ) suitable for basin-scale mapping (Jacob et al., 2022). Examples of MethaneSAT XCH4 maps from which  
 80 methane emissions data are generated can be found in Guanter et al. (2026). At a spatial resolution of  $0.04^\circ \times 0.04^\circ$   
 81 ( $\approx 4 \times 4 \text{ km}^2$ ), Level 4 (L4) emissions data from MethaneSAT are among the finest resolution among the current  
 82 swath of area flux mappers used to produce spatially-explicit emissions data products (Jacob et al., 2022). Other  
 83 satellite systems continue to play a crucial role in advancing global methane science. Global-scale inversions using

**Deleted:** are both examples of spatially-explicit methane data sources used to track progress towards methane mitigation targets

**Deleted:** Top-down

**Deleted:** of multiple instruments that improves the ability to revisit regions of the world

**Deleted:** global regional and

**Deleted:** imaging

**Deleted:** satellites like

**Deleted:** (Duren et al., 2025)

**Deleted:** . The fine spatial resolution of point source imagers allows for the identification of high-emitting point sources at  $\sim 25$ - $30$  meter pixel size

**Deleted:** (Warren et al., 2024)

**Deleted:** global mapping and area

**Deleted:** satellites

**Deleted:** coarser resolution and higher precision compared to point source imagers, with sectoral breakdowns of methane emissions available by leveraging

**Deleted:** spatially-explicit prior methane emission inventories like EDGAR and the gridded EPA-GHGI to inform the disaggregation

**Deleted:** was designed to provide methane observations at intermediate spatial scales, with

**Deleted:** in order to provide quantitative data for area emissions between the current suite of point source imagers and global flux mappers

**Deleted:** global regional and

112 GOSAT and GOSAT-2 observations produce posterior estimates of methane emissions with resolutions varying from  
113  $4.0^\circ \times 5.0^\circ$  ( $\approx 400 \times 500 \text{ km}^2$ ) (Lu et al., 2021) to  $1.0^\circ \times 1.0^\circ$  ( $\approx 100 \times 100 \text{ km}^2$ ) (Worden et al., 2022), enabling long-  
114 term global trend detection and robust atmospheric constraints while TROPOMI's nadir-viewing imaging  
115 spectrometer design provides dense global coverage that enables finer-scale posterior estimates (East et al., 2025;  
116 Qu et al., 2021; Shen et al., 2022). At regional scales, GOSAT and TROPOMI data have been demonstrated to  
117 produce finer-scaled posterior emissions estimates (Chen et al., 2023; Lu et al., 2022; Nesser et al., 2024; Varon et  
118 al., 2023; Veeffkind et al., 2023). For instance, Veeffkind et al. (2023) derived  $0.1^\circ \times 0.1^\circ$  ( $\approx 10 \times 10 \text{ km}^2$ ) emissions  
119 heatmaps in the Permian basin (US), demonstrating the strengths of these instruments when dense, high-quality (i.e.,  
120 cloud-free) observations are available. Area flux mappers continue to provide critical data on global (Shen et al.,  
121 2023; Worden et al., 2022), country/continent (Chen et al., 2023; Lu et al., 2022, 2023; Nesser et al., 2024; Shen et  
122 al., 2022), and even regional-scale emissions patterns (Varon et al., 2023; Veeffkind et al., 2023). Producing  
123 emissions estimates at even finer administrative scales (state/province, county/district or individual oil/gas fields) is  
124 more challenging with lower-resolution and moderate precision instruments, as they typically require many cloud-  
125 free observations accumulated over months to years to resolve basin and sub-basin patterns, depending on the  
126 emissions magnitude and regional observing/meteorological conditions (Shen et al., 2023). Higher-resolution  
127 mapping with high precision measurements expand the ability to characterize emissions across these important  
128 administrative boundaries (Alvarez et al., 2018; Maasackers et al., 2023; Nesser et al., 2024; Saunio et al., 2025;  
129 Schuit et al., 2023) supporting more targeted emission tracking and greater mitigation opportunity. MethaneSAT was  
130 designed to support these goals by delivering high-resolution mapping ( $\approx 4 \times 4 \text{ km}^2$ ) over substantially wider swaths  
131 (220–440 km), combined with high-precision measurements (Chan Miller et al., 2024), in turn providing an  
132 emissions tracking tool with a focus on oil and gas regions and their individual jurisdictions.

133 In this paper, we demonstrate the capabilities of MethaneSAT using a compilation of observations from six distinct  
134 regions of the world encompassing the Permian oil and gas basin, the Eagle Ford oil and gas basin, the southeastern  
135 portion of the San Joaquin Valley, Turkmenistan and Uzbekistan sections of the Amu Darya oil and gas basin, and  
136 the Zagros Foldbelt in Iran and Iraq. The regions were selected to represent a range of oil and gas production  
137 magnitudes, production characteristics (i.e., predominantly oil, gas, or a mixture of production), geography, and  
138 presence of non-oil and gas methane sources. We show sectoral allocated methane emissions for these regions and  
139 compare them to independent observations from other satellite-derived datasets and bottom-up inventories like the  
140 EPA-GHGI and EDGAR. We also analyze oil and gas normalized intensities for oil and gas methane emissions and  
141 additionally apply this analysis across administrative boundaries. Finally, we perform a detailed county/district level  
142 analysis of MethaneSAT derived emissions, highlighting the benefits of high-resolution methane emissions data, and  
143 compare those estimates to bottom-up inventories.

## 145 2 Observed regions and methane emissions analysis

### 146 2.1 Description of MethaneSAT emissions inversion process

**Deleted:** TROPOMI has substantially improved spatial coverage and temporal density, supporting posterior emission products at  $2.0^\circ \times 2.5^\circ$  ( $\approx 200 \times 250 \text{ km}^2$ ) (Qu et al., 2021) to  $0.25^\circ \times 0.25^\circ$  ( $\approx 25 \times 30 \text{ km}^2$ ) (Shen et al., 2022), and continues to be an important dataset for global methane assessments.

**Deleted:** , especially from high-emitting regions such as the Permian basin which is one of the largest emitting oil/gas basins in the US (Zhang et al., 2020)

**Deleted:** we compile a set of methane emission data products derived using

**Deleted:** MethaneSAT

**Deleted:** (Guanter et al., 2025)

**Deleted:** gridded

**Deleted:** production normalized-intensities

**Deleted:** to highlight specific areas showing large top-down/bottom-up discrepancies

164 Methane emissions inversions from MethaneSAT data produce  $0.04^\circ \times 0.04^\circ$  (i.e.,  $4 \times 4 \text{ km}^2$ ) resolution methane  
165 emission maps of total methane emissions at spatial scales of roughly  $220 \times 440 \text{ km}^2$  from a single overpass. The  
166 satellite is equipped with a pair of Littrow passive imaging spectrometers that measure the column-averaged dry-air  
167 mole fraction of methane (i.e., XCH<sub>4</sub>) at a resolution of  $\sim 110 \text{ m} \times 400 \text{ m}$  at nadir with a precision of 2.5- 5.5 ppb at  
168  $2 \times 2 \text{ km}^2$ . Methane emissions are estimated from MethaneSAT column averaged mole fractions of methane (XCH<sub>4</sub>)  
169 using the Column Observations to Regional Emissions (CORE) inversion framework, which generates the  
170 MethaneSAT Level-4 emissions product. CORE relates observed methane columns to surface fluxes through a linear  
171 forward model

$$z = J_{int} s_{int} + J_{ext} s_{ext} + (z_{prior} + Ab)$$

174 where  $z$  is the vector of observed XCH<sub>4</sub> values,  $J$  is the Jacobian matrix describing the sensitivity of each  
175 observation to surface emissions,  $s$  represents methane emission rates within the interior and exterior domains,  $z_{prior}$   
176 is the prior methane column used in the Level-2 retrieval,  $A$  is the averaging kernel, and  $b$  is a background offset  
177 parameter.

178 The source-receptor relationship represented by  $J$  is computed using the Stochastic Time-Inverted Lagrangian  
179 Transport (STILT) model (Fasoli et al., 2018; Lin et al., 2003) driven by meteorological fields from the Global  
180 Forecast System (NOAA Institutional Repository, 2026). STILT simulates backward particle trajectories from  
181 observation locations to quantify the sensitivity of each observation to upwind methane emissions. STILT footprints  
182 extend up to 28 hours back in time from the satellite observation, which is the ventilation time scale for the observed  
183 region size in typical wind conditions, while assuming constant emissions during this time.

184 MethaneSAT Level-3 observations are aggregated to  $2 \times 2 \text{ km}^2$  pixels prior to inversion to reduce measurement  
185 noise and computational cost. Emissions are estimated on a  $4 \times 4 \text{ km}^2$  grid within an interior domain defined by  
186 contiguous regions of valid observations, while potential emission sources extending up to 300 km beyond the  
187 observed domain are included to represent inflow contributions through atmospheric transport. The background  
188 methane column is represented as the retrieval prior plus an additive offset parameter scaled by the averaging kernel  
189 derived from the Level-2 methane retrieval (Chan Miller et al., 2024). Exterior emission sources are clustered  
190 according to the similarity of their transport footprints to reduce the dimensionality of the inverse problem.

191 Model parameters are estimated using Bayesian inference with state vector  $\theta = (s_{int}, s_{ext}, b)$ . Posterior samples are  
192 generated using the Stan probabilistic programming framework (Carpenter et al., 2017) with the No-U-Turn Sampler  
193 (Hoffman and Gelman, 2011), an adaptive Hamiltonian Monte Carlo algorithm (Neal, 2011). Observation  
194 uncertainty is represented by a constant standard deviation of 11 ppb, and emission rates are assigned lognormal  
195 prior distributions. Posterior mean emission rates provide the estimated flux for each grid cell, and uncertainty on  
196 the total dispersed area emissions is the 95% confidence interval from the posterior distribution ( $n=4,000$ ), with an

**Deleted:** (i.e., a “collection”)

**Deleted:** The inverse modelling system for MethaneSAT intakes XCH<sub>4</sub> observations, 617 meteorological data from the Global Forecast System (NOAA, 2015-present), a model of the topographic variation 618 in background XCH<sub>4</sub>, and an uninformative lognormal prior as inputs to the inversion process. Using the Stochastic 619 Time-Inverted Lagrangian Transport (STILT)80,81 model, we calculate a Jacobian function that links XCH<sub>4</sub> 620 enhancements to upwind sources and use the Stan software package to optimize the emissions and the background 621 concentration using the No-U-Turn Sampler (NUTS).

**Deleted:** MethaneSAT observations yield methane concentration fields that exhibit variability on different spatial scales. This variability is caused by either (a) topography in the observed region, (b) variability in the boundary inflow (i.e., the air flowing into the observed region from upwind), and (c) enhancements caused by surface fluxes within the observed region. We account for the topographic effect in the background concentration induced by a combination of the vertical atmospheric profile of methane concentration and the averaging kernel of the satellite measurement (i.e., the MethaneSAT XCH<sub>4</sub> retrieval prior) which relies on the Total Carbon Column Observing Network GGG 2020 model. The boundary inflow is a combination of the background concentration of methane and the inflow variability, the latter resulting from upwind sources and mesoscale concentration gradients. We optimize those components alongside the surface fluxes inside the observed region, using STILT model footprints to link flux rates to predicted concentration enhancements. We only report fluxes inside the observed region (“interior domain”), since those are well informed by our observations.¶

**Deleted:** Observations are aggregated to a resolution of  $2 \text{ km} \times 2 \text{ km}$  where any grid cell containing less than 50% valid data is discarded. The model optimizes the interior fluxes on a  $4 \text{ km} \times 4 \text{ km}$  grid, while the observations are aggregated to  $2 \text{ km} \times 2 \text{ km}$ . Exterior emitters are clustered in similar areas with the KMEANS algorithm based on the cosine-distance between their Jacobian footprint which reduces co-linearity between model parameters while preserving the expressivity of the boundary inflow model.

**Deleted:** This means that individual MethaneSAT emissions maps represent emissions over a duration of 28 hours, which partially addresses any variations impacted by diurnal emissions patterns in our overall estimates.

**Deleted:** on the total across all samples

244 additional 20% uncertainty added to account for assumed uncertainty in the static parameters in the input GFS  
245 weather data used for the inversions.

246

## 247 2.2 Aggregation of emissions maps and independent comparisons

248 Individual MethaneSAT emissions estimates (i.e., a MethaneSAT scene or emissions map) represent methane  
249 emission estimates up to 28 hours back in time and vary in their spatial dimensions depending on the viewing  
250 geometry of the satellite. Nadir viewing observations produce up to ~220 km wide scenes, while off-nadir  
251 observations produce up to ~440 km wide scenes. The MethaneSAT platform had an agile observing mechanism  
252 with off-nadir viewing at up to 40 degrees on one side of its observing track. We aggregate multiple MethaneSAT  
253 scenes together over the same regions to produce a spatially explicit estimate of methane emissions with increased  
254 temporal and spatial extents. To do this, we reproject all MethaneSAT emissions estimates onto a common global  
255  $0.04^\circ \times 0.04^\circ$  grid (Fig. S1) using an equal-area weighting approach that preserves total methane mass among the  
256 individual scenes. Then, we average the methane emission rates over each cell for each overlapping scene and  
257 combine to produce an aggregated methane emission heatmap. We apply the same approach using the median during  
258 aggregation as an additional test of sensitivity and find broad consistency between the two approaches (Fig. S10).  
259 We also test the sensitivity of MethaneSAT aggregated emissions estimates to the removal of single scenes and find  
260 that estimates are robust among the six regions (SI – Section 2, Fig. S12). We additionally consider any impacts  
261 from seasonal variability in our aggregated emissions estimates using 2022 monthly inversions data from  
262 TROPOMI (Pendergrass et al., 2025) to better compare to annual emissions estimates from top-down satellite  
263 inversions or bottom-up inventories (SI – Section 2).

264 We perform intercomparisons of total methane emissions estimates to other spatially explicit methane emissions data  
265 from both bottom-up and top-down methodologies. In all intercomparisons, we match the spatial domains to ensure  
266 that the same regions are being compared. In addition to total methane emissions, we also produce comparisons of  
267 available literature-based emissions from different sectors (i.e., oil and gas and non-oil and gas emissions). From the  
268 bottom-up inventories, we specifically compare MethaneSAT to the EPA-GHGI (Maasackers et al., 2023) for  
269 observations in the US, and to EDGAR - version “EDGAR\_2025\_GHG” (Crippa et al., 2024) and CAMS v6.2  
270 (Granier et al., 2019) for regions outside of the US. The EPA-GHGI provides annual estimates of methane emissions  
271 for 2020, while EDGAR and CAMS v6.2 both report annual emissions for 2024. The EPA-GHGI and EDGAR  
272 provide emissions estimates for member countries under the UNFCCC. Other bottom-up inventories that are used as  
273 prior information for satellite-based inversions include the Global Fuel Exploitation Inventory (GFEI v2) (Scarpelli  
274 et al., 2022) and CAMS v6.2 (Granier et al., 2019). Our comparisons to top-down satellite-based observations vary  
275 by region and are presented later in the Results section.

276

## 277 2.3 Sectoral disaggregation and methane intensity calculations

**Deleted:** The methodology for inversion-based MethaneSAT emission data products and related uncertainty analysis are described in Appendix A and Appendix B sections of this paper. Each

**Deleted:** or anheatmap

**Deleted:** is from a different day of observation and can be of variable dimensions depending on the viewing geometry with nadir observations leading

**Deleted:** observations

**Deleted:** observations

**Deleted:** We consider these variable observation domains over the same region of interest in our aggregation procedure of including multiple overpasses in order to produce a larger aggregated emission heatmap.

**Deleted:** To ensure consistency when aggregating repeat observations

294 We attribute MethaneSAT methane emissions to methane sectors by leveraging a combination of bottom-up  
 295 inventories and Carbon Mapper detected point sources in a composite prior inventory using a simple proportional  
 296 allocation, where  $e_i$  are MethaneSAT emissions from sector  $i$ ,  $E$  are total methane emissions estimates from  
 297 MethaneSAT,  $p_{i,j}$  are emissions estimates from prior inventory  $j$  and sector  $i$ , and  $P_j$  are total methane emissions from  
 298 prior inventory  $j$ .

299 
$$e_i = E \frac{\sum_j p_{i,j}}{\sum_j P_j}$$

300 ~~To account for structural omissions in any single inventory~~, we construct a composite dataset as the sum of multiple  
 301 independent bottom-up methane emission inventories (Fig. S5). This composite data approach has precedents in  
 302 methane inversion frameworks (Cusworth et al., 2021a; Lu et al., 2023; Shen et al., 2023) where multisource priors  
 303 or spatially-explicit inventories are used to improve completeness and robustness. For bottom-up inventories – we  
 304 incorporate the gridded EPA-GHGI (Maasackers et al., 2023), EDGAR (Crippa et al., 2024), EI-ME (Omara et al.,  
 305 2024), CAMS v6.2 (Granier et al., 2019), and GFEI v2 (Scarpelli et al., 2022) as inputs, which are all mapped at  
 306 their native spatial resolution of  $0.1^\circ \times 0.1^\circ$ . For any region ~~and sector~~, we combine emissions estimates from two  
 307 bottom-up inventories with Carbon Mapper distinct point sources to produce the composite dataset. For regions  
 308 within the US, we use the EPA-GHGI and EDGAR as inputs for non-oil and gas sources, and the EI-ME and  
 309 EDGAR for oil and gas sources. For regions outside of the US, we use CAMS v6.2 and EDGAR as inputs for non-  
 310 oil and gas sources, and the GFEI v2 and EDGAR as inputs for oil and gas sources. Other combinations of these  
 311 bottom-up inventories, and their impacts on the resulting sectoral breakdown of emissions, are provided in the SI  
 312 (Fig. S7; Fig. S8) ~~with further explanation in the SI – Section 1.1~~. We include persistence-weighted distinct point  
 313 source measurements from Carbon Mapper (Dashboard | Carbon Mapper, 2025) if they are sources that have been  
 314 observed at least three times. To better account for regions where granular oil and gas infrastructure data is limited  
 315 (i.e., regions outside of the US), we spatially aggregate oil and gas methane emissions estimates from the composite  
 316 prior by a factor of four (i.e., from the native  $0.1^\circ \times 0.1^\circ$  resolution to  $0.4^\circ \times 0.4^\circ$ ) while conserving the mass of  
 317 emissions. A sensitivity test of this approach ~~shows improved agreement in the sectoral proportions of emissions for~~  
 318 ~~non-US regions compared to a compilation of estimates from literature, while showing little to no improvement for~~  
 319 ~~regions in the US (SI – Section 1.2)~~.

320 We allocate total methane emissions estimates from MethaneSAT to broad sectors outlined as oil and gas (i.e.,  
 321 upstream and midstream sectors), waste (i.e., solid waste disposal landfills), agriculture (i.e., manure management,  
 322 enteric fermentation, and agricultural soils such as rice cultivation), coal, and other non-oil and gas sources (i.e.,  
 323 post-meter emissions, wastewater treatment, chemical processing, etc). For ~~cells where we find over 100-times the~~  
 324 total methane emissions relative to the composite ~~prior~~, we assign emissions as having an “unknown” origin and  
 325 incorporate their relative percentage contributions into the uncertainty calculations related to sectoral disaggregation.  
 326 Methane emissions from wetlands and termites are not included in the sectoral disaggregation since their combined  
 327 methane emissions are less than 1% of total methane emissions from the observed regions based on data from  
 328 WetCHARTs (v1.3.1) (Bloom et al., 2017).

**Deleted:** To reduce

**Deleted:** (Omara et al., 2024)

**Deleted:** finds that oil and gas emissions estimates increase with decreasing spatial resolution for regions outside of the US with relatively little change in oil and gas emissions estimates for regions in the US (Fig. S6).

**Deleted:** grid

**Deleted:** inventory

**Deleted:** ; Fung et al., 1991

338 We acknowledge that a wide range of measures exist under the umbrella of methane intensity (Johnson et al., 2026;  
339 Seymour et al., 2025), so we assess oil and gas methane intensity using two distinct and complementary metrics:

340 1. Marketed gas-production-normalized methane intensity, defined as the ratio of oil and gas methane  
341 emissions to marketed methane production (i.e., loss rates).

342 2. Marketed oil-and-gas-normalized methane intensity, defined as the ratio of oil and gas methane emissions  
343 to total energy production measured as marketed oil and gas production in gigajoules (GJ) (i.e., energy intensity).

344 We estimate loss rates from reported marketed natural gas production volumes, adjusted for the methane content of  
345 the produced gas, which is consistent with the oil and gas decarbonization charter's metric to track methane intensity  
346 reduction goals (OGDC - The Charter, 2025). Oil and gas production data are sourced from Wood Mackenzie for the  
347 year 2024 (Wood Mackenzie, 2025). The energy intensity metric reflects the climate impact relative to saleable  
348 energy products excluding coal and aligns with methodologies used by the International Energy Agency (IEA) for  
349 comparing methane intensities across regions (IEA, 2025). In contrast, loss rates provide a measure of a region's gas  
350 conservation performance - indicating the proportion of produced gas lost through leakage, venting, flaring, or other  
351 losses. The loss rate metric is consistent with the methane intensity frameworks established under the Oil and Gas  
352 Methane Partnership (OGMP) 2.0, supporting direct comparison between industry-reported methane targets and  
353 measurement-based assessments. We assume a methane gas composition in natural gas of 80% for loss rate  
354 calculations. Assumptions on the methane gas composition directly impact the resulting loss rate calculations which  
355 scale inversely to increasing gas composition. We test the sensitivity of our loss rate estimates using methane gas  
356 composition values from spatially-explicit estimates for the US (Burdeau et al., 2025) and approximate gas  
357 compositions for non-US regions using US basins with similar fluid production characteristics (Table S7). Energy  
358 intensity metrics do not incorporate assumptions of methane gas composition into their calculations and are  
359 therefore unaffected.

#### 360 2.4 Uncertainty in MethaneSAT scene aggregation and sectoral disaggregation

361 Uncertainty in the MethaneSAT emissions product is dominated by: 1) uncertainty in the meteorological product  
362 used to generate the STILT Jacobian that links emissions with concentrations, 2) correlated uncertainty in the  
363 observations (e.g., striping), 3) uncertainty in the background concentration, 4) uncertainty in the allocation of signal  
364 between emissions in the reported domain and the boundary inflow, and 5) uncertainty in the emission map as  
365 expressed by the variability in samples in a Markov Chain Monte Carlo (MCMC) simulation. Uncertainty in  
366 aggregated MethaneSAT emissions estimates is propagated using a Monte Carlo approach. Each emissions cell is  
367 represented by 4,000 samples drawn from its MCMC posterior distribution, reflecting mean-level uncertainty in the  
368 emissions estimate at that location. Where multiple emissions maps overlap a given cell, 4,000 combined cell-level  
369 estimates are generated by repeatedly drawing one value per map and averaging across maps. This Monte Carlo  
370 resampling procedure propagates uncertainty through the arithmetic mean without requiring assumptions about the  
371 functional form of the resulting distribution. This procedure is applied independently to all subregions defined by  
372 unique combinations of overlapping emissions maps (Fig. S2). Uncertainty on the total dispersed area emissions is

**Deleted:** -normalized

**Deleted:** -normalized

**Deleted:** gas production-normalized methane intensity (i.e., loss rate)

**Deleted:** This metric, normalized by marketed gas production,

**Deleted:** all intensity metric

**Deleted:** We use a bootstrap resampling of the MCMC samples to estimate uncertainty for methane emissions for each emissions map, with propagation of uncertainty from each of the above effects by either sweeping across values of input parameters (e.g., recomputing the inversions with high and low estimates of the mean background concentration) or modifying each sample (e.g., errors in the wind speed data).

387 the 95% confidence interval on the total across all samples ( $n = 4,000$ ), with an additional 20% uncertainty added to  
388 account for assumed uncertainty in the static parameters in the input GFS weather data used for the inversions.

389 To calculate uncertainties related to the disaggregation of methane emissions by sector, we bootstrap with  
390 resampling ( $n = 4,000$ ) the input data used to create the prior emissions estimates in our stacked prior inventory,  
391 which are in turn used to re-calculate the disaggregation of methane emissions. For the bottom-up inventories,  
392 regardless of sector, we assume a normal distribution with a standard deviation of 50% for the cell-level emissions  
393 estimates. For the Carbon Mapper point sources, we use the provided source-level standard deviations assuming a  
394 normal distribution to resample the emission rates ( $n=4,000$ ). Sectoral ratios of methane emissions are then  
395 calculated 4,000 times using these resampled input data to provide upper and lower bounds on the uncertainty for  
396 the associated sectoral methane emissions, which we then use to obtain the 97.5<sup>th</sup> and 2.5<sup>th</sup> percentiles as the sectoral  
397 disaggregation uncertainty including the added relative contributions of unknown methane emissions to the total.  
398 The additional uncertainty relating to the attribution of unknown methane emissions from MethaneSAT contributes  
399 only <1% of uncertainty to the total for the regions we analyze in this work.

400  
401

## 402 2.5 Region descriptions

403 We present MethaneSAT observations from six distinct regions intersecting six countries, seven major oil and gas  
404 producing basins, and 207 districts/counties (i.e., Level 2 data from the Global Administrative Areas database –  
405 GADM). All regions are named according to the primary oil and gas basin encompassed by MethaneSAT  
406 observations (Table S1), even if the full basin is not contained within the full observation domain.

407 Regions A, B, and C, are all located in North America, mostly in the [United States \(US\)](#). Region A (i.e., “Permian”  
408 observation domain) covers the oil-dominant Permian basin (i.e., >50% of combined energy production is from oil)  
409 (Fig. S9), one of the highest producing basins in the world with a long legacy of resource development and a  
410 sustained production surge beginning in the 2010’s, leading to significant growth in associated infrastructure  
411 development (Scanlon et al., 2017). Region B (i.e., the “San Joaquin” observation domain) targets the state of  
412 [California \(US\) encompassing regions with elevated methane emissions associated with a mixture of oil and gas](#)  
413 [activity, landfills, and livestock-related agricultural activity \(Duren et al., 2019; Miller et al., 2015; Vecchi et al.,](#)  
414 [2023\)](#). The San Joaquin basin is a mature oil-dominant basin (Fig. S9) with production dating back to the late  
415 1800’s, with many older wells presently active. Region C (i.e., the “Eagle Ford” observation domain) principally  
416 targets the Eagle Ford oil and gas basin in the US, but also extends into Mexico with some coverage of the Sabinas  
417 basin where coal production first began in the country (Dávila-Pulido et al., 2023). The Eagle Ford oil and gas basin  
418 is one of the youngest hydrocarbon basins we analyze in this work, with the first wells drilled in the late 2000’s and  
419 an overall balance of oil versus gas production (Fig. S9).

**Deleted:** We calculate uncertainties in the aggregated regional-level estimates by stacking the results of the 4,000 samples from the MCMC simulations for each emissions cell. Where multiple emissions maps find emissions for the same cell, then we randomly resample from these emissions maps and average cell-level emissions estimates across layers to obtain 4,000 estimates of an aggregated mean value representing the estimated methane emissions within that subregion. We perform this sub-regional averaging and aggregation across all areas with unique combinations of emissions maps (Fig. 1). We then add all total methane estimates for each subregion across all 4,000 samples to calculate the 97.5th and 2.5th percentiles of the total methane emissions of the entire aggregated spatial domain. ¶

**Deleted:** Notable, this

**Deleted:** In this study, we

**Deleted:** 99% of total oil and gas production within the Permian oil and gas basin23 by combining a total of nine MethaneSAT observations with repeat coverage over the Midland and Delaware sub-basins, both associated with most of the oil and production in the larger Permian basin. The Permian basin, which is one of the highest producing basins in the world, is

**Deleted:** (Guanter et al., 2025)

**Deleted:** combines six observations over two distinct regions of the San Joaquin Valley - the Kings and Tulare counties which have been previously identified as regions with elevated methane emissions associated with livestock-related agricultural activity, and the Kern county associated with a mixture of oil and gas activity, landfills, and agricultural activity. ...

**Deleted:** oil and gas

**Deleted:** highly

**Deleted:** Oil and gas production within the San Joaquin basin has been steadily declining over the past four decades (EIA-914 monthly production report, 2025).

**Deleted:** utilizes three observations that

457 Regions D, E, and F are all located in Asia and the Middle East. Region D (i.e., “Amu Darya – UZB”) covers most  
458 of the province of Qarshi (Uzbekistan) with some overlap into Turkmenistan. The Amu Darya – UZB region  
459 overlaps the Amu Darya oil and gas basin and encompasses multiple oil and gas fields along the border of  
460 Uzbekistan and Turkmenistan (Yu et al., 2015). Region E (i.e., “Amu Darya – TKM”) covers a separate portion of  
461 the Amu Darya basin that contains several major gas fields (Yu et al., 2015) and the city of Mary, the fourth largest  
462 city in Turkmenistan. The Amu Darya basin itself is predominantly gas-producing (i.e., >90% of combined  
463 production is gas) (Fig. S9). Region F (i.e., “Zagros Foldbelt”) targets the Zagros Foldbelt oil and gas basin in Iran,  
464 with partial coverage over the Widyān oil and gas basin in Iraq (Fig. S2). The Zagros Foldbelt basin is a large oil-  
465 dominant basin (Fig. S9) with a long history of oil and gas production dating back to the early/mid 1900’s (Alipour,  
466 2024).

467

### 468 3 Results

469 We incorporate a total of 33 MethaneSAT scenes from six separate regions of the world including the United States  
470 (US), Mexico, Turkmenistan, Uzbekistan, Iran, and Iraq (Table S1). The observation dates of MethaneSAT data span  
471 one year from May 2024 to May 2025. Total methane emissions from the single scenes range from 353 (95% c.i.:  
472 268 - 446) t h<sup>-1</sup> in the Permian oil and gas basin in October 2025, to 29 (95% c.i.: 16 – 46) t h<sup>-1</sup> measured in the  
473 Eagle Ford oil and basin in December 2024 (Table S1). The seasonal representativity of the individual scenes are  
474 discussed in the SI – Section 2 (Fig. S13). We aggregate these single scenes together to form regional estimates of  
475 methane emissions. In the US, the aggregated MethaneSAT observation domains capture 99% of total onshore oil  
476 and gas production for 2024 in the Permian and San Joaquin regions, and 66% of onshore production in the Eagle  
477 Ford (Fig. S9) (Wood Mackenzie, 2025). Outside of the US, the aggregated MethaneSAT observation domains cover  
478 58% of total onshore oil and gas production in the Zagros Foldbelt, and 79% of total onshore oil and gas production  
479 from the Amu Darya oil and gas basin from the combined observations in Uzbekistan and Turkmenistan (Fig. S9).  
480 Cumulatively, the six regions account for 11% of global onshore oil and gas production for 2024 (Wood Mackenzie,  
481 2025).

482

#### 483 3.1 Methane emissions by region and sector

484 Total methane emissions for the regional six observations domains are: 454 t h<sup>-1</sup> (95% c.i.: 351 – 563) in the  
485 Permian, 251 t h<sup>-1</sup> (95% c.i.: 189 – 321) in the Zagros Foldbelt, 192 t h<sup>-1</sup> (95% c.i.: 146 – 242) in Amu Darya –  
486 UZB, 188 t h<sup>-1</sup> (95% c.i.: 141 – 239) in Amu Darya – TKM, 127 t h<sup>-1</sup> (95% c.i.: 95 – 162) in the San Joaquin, and  
487 114 t h<sup>-1</sup> (95% c.i.: 83 – 149) in the Eagle Ford (Fig. 1).

488 We attribute methane emission estimates from MethaneSAT to specific methane sectors and find varied sectoral  
489 emissions among the different observation domains, reflecting a diversity of methane emitting sources among the  
490 different regions. The Permian contains the highest percentage of oil and gas methane emissions at 90% (95% c.i.:  
491 64 – 100%), followed by the Zagros Foldbelt at 81% (95% c.i.: 58 – 100%), the Eagle Ford at 70% (95% c.i.: 41 –

Deleted: combines six MethaneSAT scenes covering

Deleted: In

Deleted: , we aggregate four scene that also

Deleted: containing

Deleted: dominated by gas production

Deleted: , with the first productive gas fields discovered around the 1950’s before development continued throughout the 1960’s to 1980’s (Ulmishek, 2004).

Deleted: For

Deleted: we combine six scenes in

Deleted: with periodical investments stimulating modernization in the basin, producing a mixture of legacy and upgraded infrastructure

Deleted: in the United States (USA) at

Deleted: emission heatmaps

Deleted: (see Methods - Section 2.2)

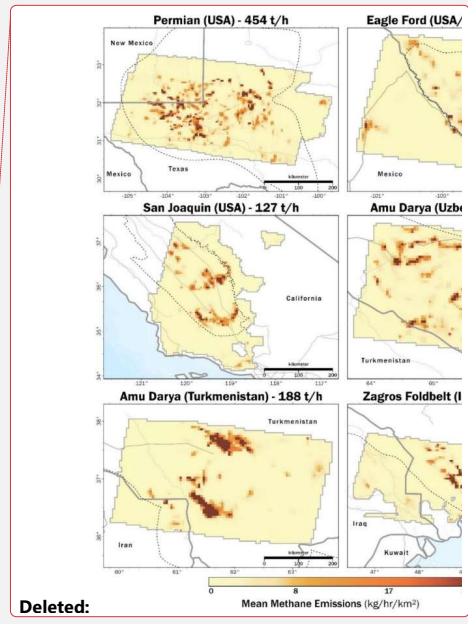
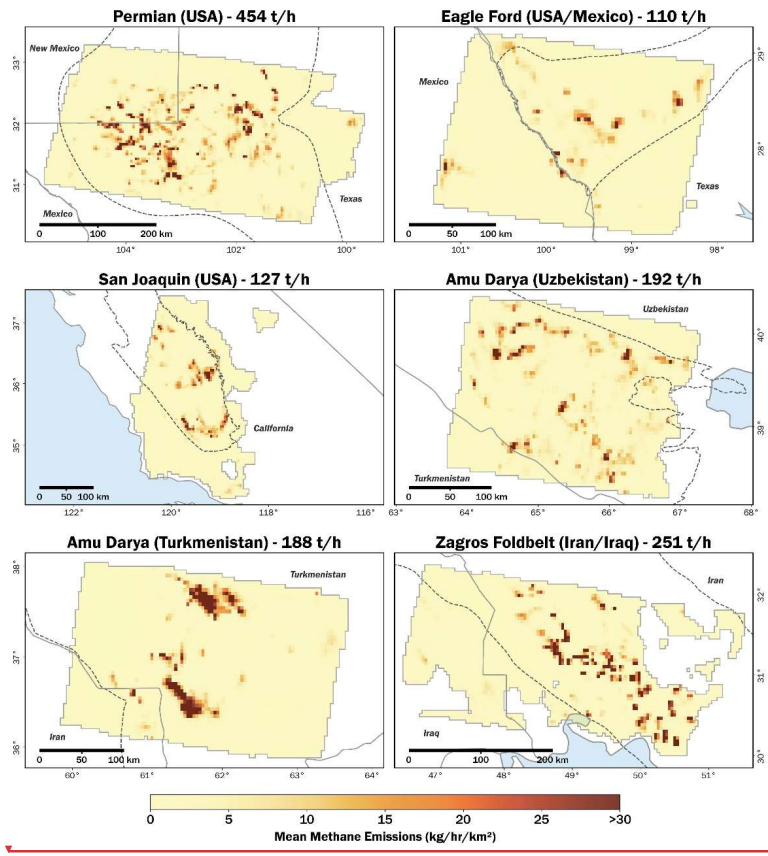
Deleted: (WoodMac, 2025)(Lens: Natural Resources Data Analytics Platform, 2025)

510 99%), Amu Darya – UZB at 52% (95% c.i.: 37 – 70%), Amu Darya – TKM at 52% (95% c.i.: 38 – 66%), and the  
 511 San Joaquin at 24% (95% c.i.: 18 – 31%) (Fig. 2). Among non-oil and gas sources, the dominant sector was  
 512 consistently agricultural emissions associated with livestock like concentrated animal feeding operations (i.e.,  
 513 CAFO's) and manure management (Fig. 2). After the agricultural sector, non-oil and gas emissions from the waste  
 514 and other (i.e., wastewater treatment, post-meter, stationary combustion, etc) sources were the most prominent  
 515 emission sectors in Amu Darya – UZB, Amu Darya – TKM, Zagros Foldbelt, and San Joaquin (Table S2). For the  
 516 Eagle Ford region, the waste and coal sectors were the highest methane-emitting sectors from non-oil and gas  
 517 sources after the agricultural sector. Detailed sectoral emissions estimates are shown in Table S2.

**Deleted:** with the lowest percentage of oil and gas emissions ...

**Deleted:** among the observation domains

**Deleted:** by region can be found



**Deleted:**

518  
 519  
 520 **Fig. 1:** Maps of aggregated MethaneSAT methane emissions from the Permian (US), Eagle Ford (US, Mexico), San  
 521 Joaquin (US), two separate Amu Darya regions in Turkmenistan and Uzbekistan, and the Zagros Foldbelt (Iran,  
 522 Iraq). Notable geographical boundaries are illustrated in the maps, including country boundaries in solid grey, and  
 523 oil and gas basin boundaries in dashed outlines.

530 We calculate methane intensities based on marketed gas (i.e., loss rates) and total oil and gas (i.e., energy intensity)  
 531 production for 2024 (Wood Mackenzie, 2025) from all aggregated domains and for notable administrative/sub-basin  
 532 boundaries among the observation domains (Fig. 3). Loss rates among the six regions consistently exceed the 0.2%  
 533 goal set within the Oil and Gas Climate Initiative by factor of ten (Oil and Gas Climate Initiative | OGCI, 2025). The  
 534 Eagle Ford region has the lowest loss rates at 2.4% (95% c.i.: 1.4 – 3.4%), followed by the Permian at 2.6% (95%  
 535 c.i.: 1.9 – 3.5%), Amu Darya – TKM region at 2.9% (95% c.i.: 2.1 – 3.7%), Amu Darya – UZB region at 3.7% (95%  
 536 c.i.: 2.7 – 5.0%), the San Joaquin region at 12.1% (95% c.i.: 8.9 – 16.0%), and the loss rates in the Zagros Foldbelt  
 537 at 18.6% (95% c.i.: 13.4 – 23.8%). For energy intensities, which accounts for combined marketed oil and gas  
 538 production, we estimate the lowest energy intensities for the Zagros Foldbelt at 0.16 (95% c.i.: 0.12 – 0.20) kg CH<sub>4</sub>  
 539 GJ<sup>-1</sup> and the Permian at 0.16 (95% c.i.: 0.12 – 0.21) kg CH<sub>4</sub> GJ<sup>-1</sup>, followed by the Eagle Ford at 0.21 (95% c.i.: 0.12  
 540 – 0.30) kg CH<sub>4</sub> GJ<sup>-1</sup>, the Amu Darya – TKM region at 0.40 (95% c.i.: 0.29 – 0.51) kg CH<sub>4</sub> GJ<sup>-1</sup>, the San Joaquin  
 541 region at 0.42 (95% c.i.: 0.31 – 0.55) kg CH<sub>4</sub> GJ<sup>-1</sup>, and the highest energy intensities in the Amu Darya – UZB  
 542 region at 0.51 (95% c.i.: 0.27 – 0.69) kg CH<sub>4</sub> GJ<sup>-1</sup>. We observe similar intensity metrics, both for loss rates and  
 543 energy intensities, within the specific spatial domains of oil and gas basin boundaries compared to the full  
 544 observation domains (Fig. 2; Table S3).

545 We compare methane emissions estimates and methane intensities across sub-basins and administrative boundaries  
 546 (e.g., countries/states) (Fig. 2). Within the Delaware and Midland subbasins of the Permian (Fig. 2), we estimate oil  
 547 and gas methane emissions of 178 t h<sup>-1</sup> (95% c.i.: 132 – 224) and 112 t h<sup>-1</sup> (95% c.i.: 81 – 143) respectively, with  
 548 comparable marketed loss rates of 2.0%. The Permian basin transects both the New Mexico and Texas state  
 549 boundaries, where we estimate oil and gas methane emissions of 67 t h<sup>-1</sup> (95% c.i.: 43 – 90) and 338 t h<sup>-1</sup> (95% c.i.:  
 550 249 – 427) respectively. We find over twice the loss rates and energy intensities values in Texas at 3.1% and 0.19 kg  
 551 CH<sub>4</sub> GJ<sup>-1</sup> compared to New Mexico at 1.3% and 0.08 kg CH<sub>4</sub> GJ<sup>-1</sup> (Fig. 2; Table S3). The same state-level  
 552 comparison restricted to the Delaware subbasin boundary shows a similar contrast in methane intensities with the  
 553 Texas portion of the Delaware subbasin having a loss rate of 2.8% compared the New Mexico portion of the  
 554 Delaware subbasin at 1.0%. Similar trends have also been observed in recent TROPOMI-based estimates by Varon  
 555 et al. (2025), with New Mexico showing decreasing loss rates from 4.5% in 2019 to 2.1% in 2023 plausibly  
 556 associated with state-wide policies requiring operators to reduce methane intensities below 2% by 2026 (N.M. Code  
 557 R. § 19.15.27.9 Statewide Natural Gas Capture Requirements, 2025).

558 In the Eagle Ford, we note that nearly all oil and gas emissions occur within the US compared to Mexico, with  
 559 methane emissions in Mexico largely originating from agricultural sources and coal (Fig. 2; Table S6). Nearly all oil  
 560 and gas infrastructure is located within the Eagle Ford oil and gas basin boundary, with sparse infrastructure in  
 561 Mexico compared to the US (Omara et al., 2023). MethaneSAT observations in Mexico largely transect the Burgos  
 562 basin, a major natural gas-producing basin. Although geologically similar to the Eagle Ford basin, daily gas  
 563 production in the Eagle Ford exceeds 7,000 MMcf day<sup>-1</sup> compared to 30 MMcf day<sup>-1</sup> from the Burgos, highlighting  
 564 stark differences in the degree of development between the basins which we can clearly observe in the oil and gas

Deleted: energy

Deleted: combined oil and gas

Deleted: measured in this work

Deleted: highest gas-production normalized

Deleted: -normalized methane

Deleted: -normalized

Deleted: -production normalized methane

Deleted: marketed gas-production and oil and gas-production normalized intensity

Deleted: specific

Deleted: broader

Deleted: Midland

Deleted: Delaware

Deleted: gas-production normalized

Deleted: from MethaneSAT observations

Deleted: marketed gas- and energy-production normalized methane intensity

Deleted: discrepancy

Deleted: the magnitude of the

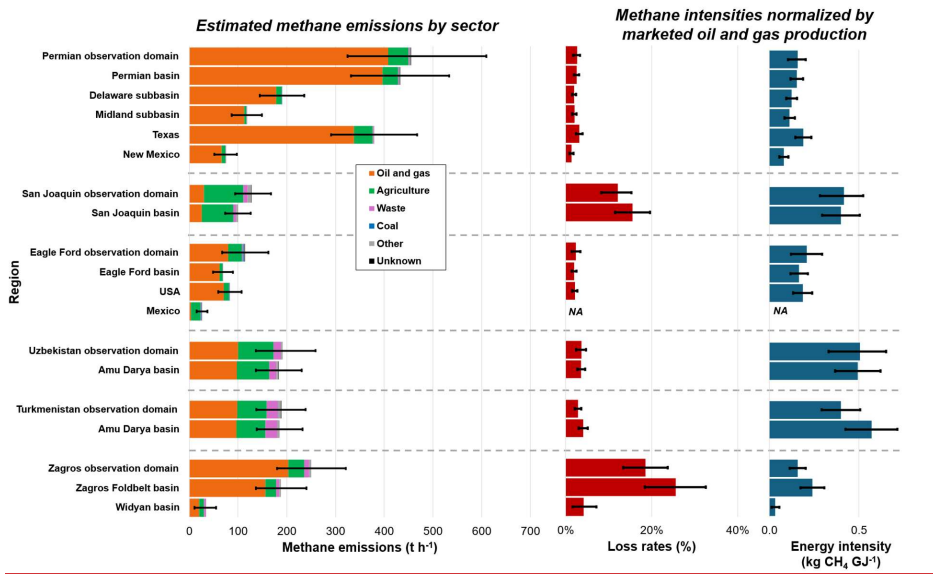
Deleted: marketed gas-production normalized intensity

Deleted: methane intensities

Deleted: similar to

methane emission estimates from MethaneSAT. We find that the methane intensities in the Zagros Foldbelt oil and gas basin in Iran (i.e., 25.5% and 0.24 kg CH<sub>4</sub> GJ<sup>-1</sup>) are over five-times higher than the bordering Widyan oil and gas basin in Iraq (i.e., 4.2% and 0.03 kg CH<sub>4</sub> GJ<sup>-1</sup>), noting that MethaneSAT observations only cover 17% of combined oil and gas production in the Widyan basin compared to 58% from the Zagros Foldbelt basin (Fig. S9). Within the Amu Darya basin boundary, we find higher methane intensities from the Amu Darya – TKM region at 4.1% and 0.57 kg CH<sub>4</sub> GJ<sup>-1</sup> compared to the Amu Darya – UZB at 3.6% and 0.49 kg CH<sub>4</sub> GJ<sup>-1</sup> (Table S3). Collectively, MethaneSAT observations from the Amu Darya basin have an associated loss rate intensity of 3.8% and an energy intensity of 0.53 kg CH<sub>4</sub> GJ<sup>-1</sup>.

595



596

597 **Fig. 2:** Sectoral breakdown of methane emissions from aggregated MethaneSAT emissions for full observation  
 598 domains, and subregions defined by administrative boundaries and oil and gas basin and sub-basins. Methane  
 599 intensities normalized by marketed gas- (i.e., loss rate) and oil-and-gas- (i.e., energy intensity) production are  
 600 calculated for all observation domains and subregions. (Wood Mackenzie, 2025).

601

602

603

604 **3.2 Comparison of MethaneSAT-derived emissions to independent estimates**

605 Our estimates of methane emissions and sectoral breakdowns from MethaneSAT match closely with other

606 independent estimates for the same spatial domains from other satellite observations (Fig. 3). The Permian basin has

Deleted: 9

Deleted: – TKM and Amu Darya – UZB cover 79% of total oil and gas production within the Amu Darya oil and gas basin(Wood Mackenzie, 2025) (Fig. S9) with

Deleted: gas-production normalized

Deleted: -normalized

Deleted: including

Deleted: production

Deleted: normalized intensities

Deleted: energy

Deleted: -normalized

Deleted: production intensities

Deleted: In the Permian basin, a

Deleted: region that

621 been extensively surveyed using a wide range of methods from ground-based surveys (Robertson et al., 2020; Yu et  
622 al., 2022), tower-based observations (PermianMAP, 2025; Barkley et al., 2023), aerial-based surveys (Chen et al.,  
623 2022; Cusworth et al., 2021b; Hmiel et al., 2023; Sherwin et al., 2024), and satellite-based observations (Cusworth  
624 et al., 2022; Irakulis-Loitxate et al., 2021; Lu et al., 2022; Nesser et al., 2024; Shen et al., 2022; Varon et al., 2025;  
625 Worden et al., 2022). We find that our estimate of oil and gas emissions in the Permian of 408 t h<sup>-1</sup> (95% c.i.: 303 -  
626 516) for 2024 are similar to recent TROPOMI inversions by Varon et al. (2025) and East et al. (2025), and generally  
627 higher than older satellite-based estimates from 2020 and 2019 (Fig. 3). Our estimated marketed gas-production  
628 normalized methane intensity within the Permian basin domain of 2.5% (95% c.i.: 1.9 – 3.1%) for the Permian  
629 closely aligns with recent estimates from MethaneAIR for 2023 at 2.4% (95% c.i.: 1.5 – 3.2%) (MacKay et al.,  
630 2026) (Table S3), noting that methane intensities from MethaneAIR are calculated using gross gas production  
631 instead of marketed gas production. Our estimate of non-oil and gas emissions in the Permian region of 41 t h<sup>-1</sup>  
632 (95% c.i.: 26 - 75) closely matches recent TROPOMI based inversions from 2023 (East et al., 2025; Varon et al.,  
633 2025), but higher than older estimates from GOSAT (Lu et al., 2023; Worden et al., 2022).

Deleted: the most

Deleted: estimates from

Deleted: the most recent comparable dataset from Varon et al. (2025) of 48 t/h

634 In the Eagle Ford region, we find that our total emissions estimate of 114 t h<sup>-1</sup> (95% c.i.: 83.6 - 150) is higher than  
635 most other independent satellite-based observations (Fig. 3) with differences largely attributable to higher oil and  
636 gas emission estimates from MethaneSAT. Our estimated loss rates within the Eagle Ford of 1.9% (95% c.i.: 1.3 –  
637 2.8%) closely matches recent MethaneAIR measurements from 2023 of 2.0% (95% c.i.: 1.6 – 2.7%) (MacKay et al.,  
638 2026), noting our use of marketed versus gross gas production. We find no strong seasonal biases in our methane  
639 emissions estimates for the Eagle Ford (SI – Section 2, Table S6), implying that the differences between top-down  
640 estimates are reflective of the observed methane emissions.

Deleted: marketed gas production-normalized loss rate

641 In the San Joaquin region, we estimate 30 t h<sup>-1</sup> (95% c.i.: 20 – 41) from oil and gas sources which compares well  
642 with multiple independent satellite-based estimates (Fig. 3). We find elevated loss rates within the San Joaquin oil  
643 and gas basin boundary at 15.5% (95% c.i.: 11.4 – 19.6%), which is also observed in Omara et al. (2024) with a loss  
644 rate of 15.3% for the entire San Joaquin oil and gas basin in 2021. The San Joaquin basin is characterized by a large  
645 proportion of marginally-producing well sites (Omara et al., 2018), which are typically associated with increased  
646 methane loss rates (Omara et al., 2022). We find higher emissions from non-oil and gas sources (i.e., 97 t h<sup>-1</sup>) within  
647 the San Joaquin region compared to older satellite-based estimates (Lu et al., 2023; Worden et al., 2022),  
648 additionally noting that the aggregated MethaneSAT estimates may underestimate emissions by ~10% based on the  
649 seasonal timing of the scene collections (SI – Section 2; Table S6). We further note that our measurements were  
650 performed during daylight hours, which would also influence comparisons with annual average inventory estimates  
651 for the San Joaquin (SI – Section 2).

Deleted: , implying that the elevated emission observations from MethaneSAT may reflect increasing natural gas production in recent years, especially from the Austin Chalk Play where natural gas production has nearly quadrupled since 2014 (EIA-914 monthly production report, 2025).

Deleted: marketed gas-production normalized

Deleted: gas production-normalized methane intensity

Deleted: Cui et al., 2017;

652 In the Amu Darya – UZB region, our estimates of oil and gas emissions at 100 t h<sup>-1</sup> (95% c.i.: 57 – 137) support the  
653 higher range of 39 to 110 t h<sup>-1</sup> (Fig. 3) found in independent satellite-based estimates. Oil and gas production within  
654 Uzbekistan has stabilized/declined in past decades (Uzbekistan - Countries & Regions, 2025), supporting similar oil  
655 and gas methane emission estimates from past satellite-based inversions to estimates from MethaneSAT (Fig. 3).  
656 Our estimates of non-oil and gas emissions from the Amu Darya region of 92 (95% c.i.: 55 – 134) t h<sup>-1</sup> exceed those

Deleted: (Fig. 3), which may reflect changes in the dairy industry for the region. While oil and gas production has declined in recent decades, milk production has grown 153% in the state of California since the early 1980's, with most of the growth occurring within Tulare county (Barrowman et al., 2025).

676 from independent estimates which range from ~~13~~ to ~~39~~  $t h^{-1}$  (Fig. 3). Our total methane emission estimates from the  
677 Amu Darya – UZB region are also higher than other independent estimates, albeit with statistical overlap for  
678 estimates from GOSAT estimates in North Africa (Western et al., 2021) and TROPOMI estimates in the Middle East  
679 and North Africa (Chen et al., 2023). Annual trends for methane emissions in Uzbekistan, as reported to the  
680 UNFCCC from 1990-2012 (UNFCCC, 2025), indicate increasing emissions from non-oil and gas sources like  
681 enteric fermentation, landfills, and wastewater treatment versus declining/stable emissions from the energy sector.  
682 Estimates from MethaneSAT for the Amu Darya – UZB region may indicate a continuation of these trends.

683 In the Amu Darya – TKM region, we find ~~close agreement to recent TROPOMI inversions from 2023 for both oil~~  
684 ~~and gas and non-oil and gas emissions~~ (East et al., 2025). Only one other satellite-based ~~estimate~~ contains full  
685 sectoral emissions for the region (Worden et al., 2022), which finds negligible non-oil and gas emissions (Fig. 3).  
686 Non-oil and gas emissions from the Amu Darya – TKM region are predominantly from agricultural and waste  
687 sectors respectively at  $60 t h^{-1}$  (95% c.i.: 38 – 85) and  $24 t h^{-1}$  (95% c.i.: 15 – 32) located in the North of the  
688 observation domain over the city of Mary (Fig. 1). Our estimates of ~~loss rates~~ in the Amu Darya – TKM region of  
689 2.6% (95% c.i.: 1.7 – 3.6%) ~~are~~ lower than the 4.9% estimated from satellite-based observations for 2019 (Chen et  
690 al., 2023), although the MethaneSAT observations exclude the South Caspian area, a region that has been repeatedly  
691 observed with large point source emissions associated with oil and gas infrastructure (Irakulis-Loitxate et al., 2021;  
692 Varon et al., 2021).

693 Our total methane emission estimates from the Zagros Foldbelt region overlap with multiple satellite-based  
694 observations (Fig. 3), although we estimate higher emissions attributable to non-oil and gas sources compared to  
695 ~~other~~ satellite-based ~~estimates~~ that provide comprehensive sectoral disaggregation of methane emissions for the  
696 region (East et al., 2025; Worden et al., 2022). Our estimates of oil and gas emissions are ~~within the range of other~~  
697 ~~satellite-based estimates for the region (Fig. 3)~~. We find high ~~loss rates~~ in the Zagros Foldbelt oil and gas basin at  
698 25.5% (95% c.i.: 18.5 – 32.6%), which is over ten-times higher than country level estimates of 0.8% for Iran from  
699 satellite-based observations from 2019 (Chen et al., 2023). A comparison of methane emissions estimates within the  
700 MethaneSAT observation domain from the same study (Chen et al., 2023) are less than half the emissions estimated  
701 by MethaneSAT, which could contribute to the observed differences in methane intensities, in addition to other  
702 factors (i.e., variations in the spatial representation of the loss rate estimates, production characteristics, sectoral  
703 disaggregation methods, and study year).

Deleted: 14

Deleted: 45

Deleted: (Greenhouse Gas Inventory Data - Detailed data by Party, 2025)

Deleted: consistently higher estimates of methane emissions from MethaneSAT compared to other satellite-based observations

Deleted: observation

Deleted: from GOSAT observations

Deleted: marketed gas-production normalized methane intensity metrics

Deleted: Worden et al. (2022) which is the only

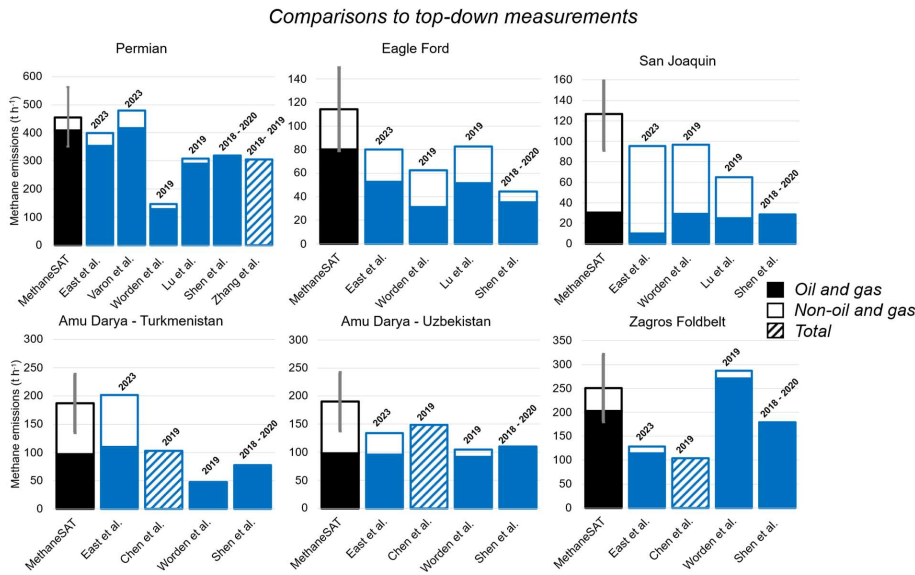
Deleted: observation

Deleted: lower than both Shen et al. (2023) and Worden et al. (2022), which could indicate declining oil and gas emissions in the region

Deleted: However, this contradicts production trends in both Iran and Iraq which both show increasing gas production over the past decade based on the International Energy Agency (IEA, 2025) (Iraq - Countries & Regions, 2025; Iran - Countries & Regions, 2025).

Deleted: marketed gas production normalized

726

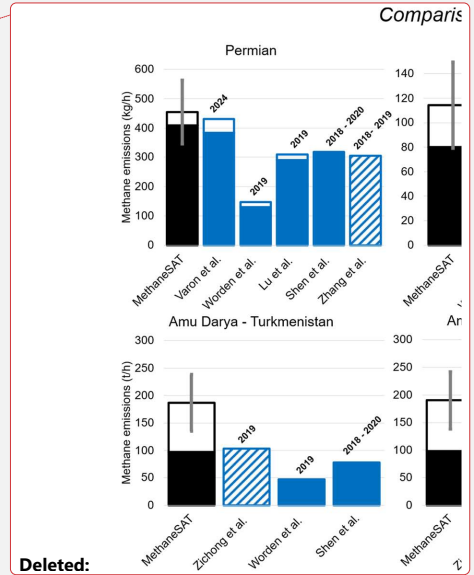


727

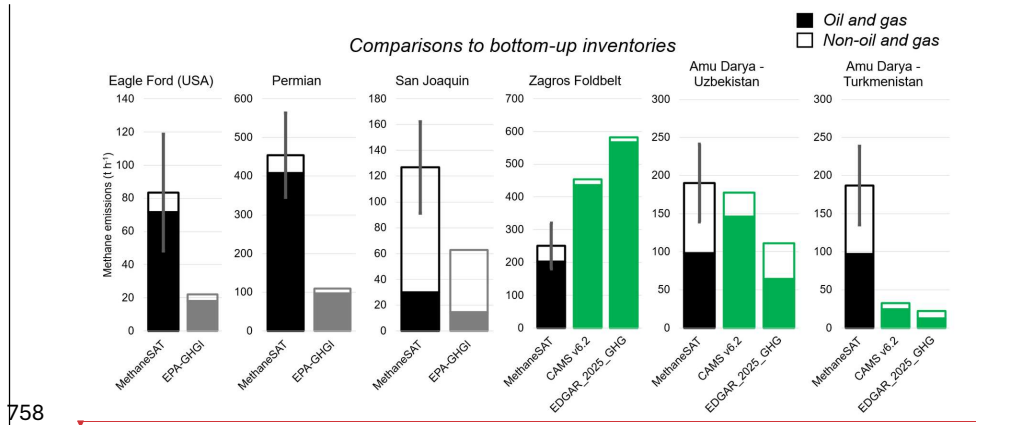
728 **Fig.3:** Comparisons of oil and gas and non-oil and gas methane emission estimates from MethaneSAT to recent (i.e.,  
 729 post-2018) independent top-down observations from peer-reviewed studies. Measurements years are indicated above  
 730 the bars. The number of available top-down studies available for comparison vary by region, with the highest  
 731 number of independent estimates available for the Permian region. Note that emission estimates from Shen et al.  
 732 (2023) are only associated with the oil and gas and coal sectors. Independent studies that do not disaggregate  
 733 methane emissions by sector are indicated by dashed bars.

734

735 In the US, we find that MethaneSAT observations from 2024-2025 are consistently higher than 2020 estimates from  
 736 the gridded EPA-GHGI by a factor of 2-5. This finding echoes recent results from comprehensive aerial sampling  
 737 campaign from MethaneAIR\_(MacKay et al., 2026), and a broader trend of top-down observations exceeding  
 738 estimates from bottom-up inventories (Sauniois et al., 2025). We find that both oil and gas, and non-oil and gas  
 739 emissions estimates from MethaneSAT exceed those from the gridded EPA-GHGI, highlighting broad discrepancies  
 740 among multiple methane-emitting sectors. Oil and gas emissions estimates from MethaneSAT are four-times higher  
 741 compared to the gridded EPA-GHGI in the Permian and Eagle Ford regions and two-times higher in the San  
 742 Joaquin. Emissions from the waste sector are consistent between MethaneSAT and the gridded EPA-GHGI, with  
 743 most differences from non-oil and gas sources occurring from the agricultural sector with MethaneSAT finding  
 744 higher estimates by a factor of four in the Eagle Ford and Permian, and a factor of two in the San Joaquin. For all  
 745 three regions in the US, oil and gas emissions were consistently higher than the EPA-GHGI by a greater degree  
 746 when compared to non-oil and gas emissions.



748 For regions outside of the US, we compare MethaneSAT observations to bottom-up emission inventories from  
 749 EDGAR (Crippa et al., 2024) and CAMS v6.2 (Granier et al., 2019). For the Zagros Foldbelt, we find closer  
 750 agreement to CAMS v6.2 compared to EDGAR. In Amu Darya – UZB, we find comparable estimates of oil and gas  
 751 emissions from EDGAR and CAMS v6.2, but our estimates of non-oil and gas emissions are twice as high as the  
 752 bottom-up estimates, largely due to increased emissions related to agriculture. We see the largest discrepancies  
 753 between MethaneSAT and bottom-up inventories in the Amu Darya – TKM region, with MethaneSAT estimates of  
 754 methane emissions more than five-times higher than the 33 and 22  $t h^{-1}$  estimated within CAMS v6.2 and EDGAR  
 755 respectively (Fig. 4). Persistence-adjusted point source detections from Carbon Mapper alone amount to 20  $t h^{-1}$  in  
 756 the Amu Darya – TKM region (Fig. S4), implying that bottom-up estimates are likely underestimating emissions in  
 757 the region.



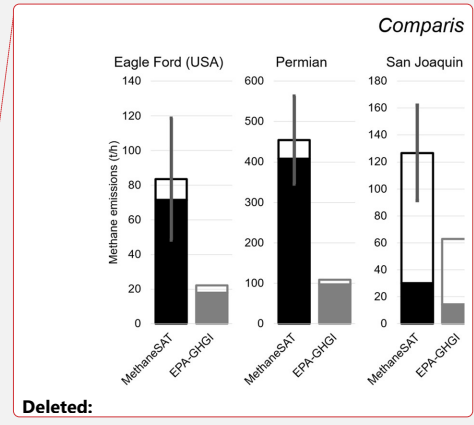
758  
 759 **Fig. 4:** Comparisons of oil and gas and non-oil and gas methane emission estimates from MethaneSAT to bottom-up  
 760 inventories. In the US, we compare MethaneSAT emission estimates to the EPA-GHGI which is a national  
 761 greenhouse gas inventory used to report methane emissions and inform policy. For regions outside of the US, we  
 762 compare MethaneSAT emissions to CAMS v6.2 and EDGAR\_2025\_GHG, both global bottom-up methane  
 763 emissions datasets that are commonly used to inform prior emissions estimates in top-down inversions. Note that for  
 764 the Eagle Ford region, we restrict our comparison to the EPA-GHGI only for the region contained in the US, hence  
 765 the lower total emissions estimates compared to the full observation domain.

766

767 **3.3 Insights from MethaneSAT emissions estimates across jurisdictions**

768 We quantify methane emissions from MethaneSAT for jurisdictions (i.e., second-level administrative divisions -  
 769 county/districts) from all six regions analyzed in this work. We investigate differences between bottom-up inventory  
 770 estimates within jurisdictional bounds using the high-resolution data provided from MethaneSAT observations.

771 In the Permian region, the five highest emitting counties (i.e., Reeves, Eddy, Culberson, Lea, and Pecos) collectively  
 772 contribute 41% of total methane emissions from the region (Fig. 5). We find that total methane emissions estimates

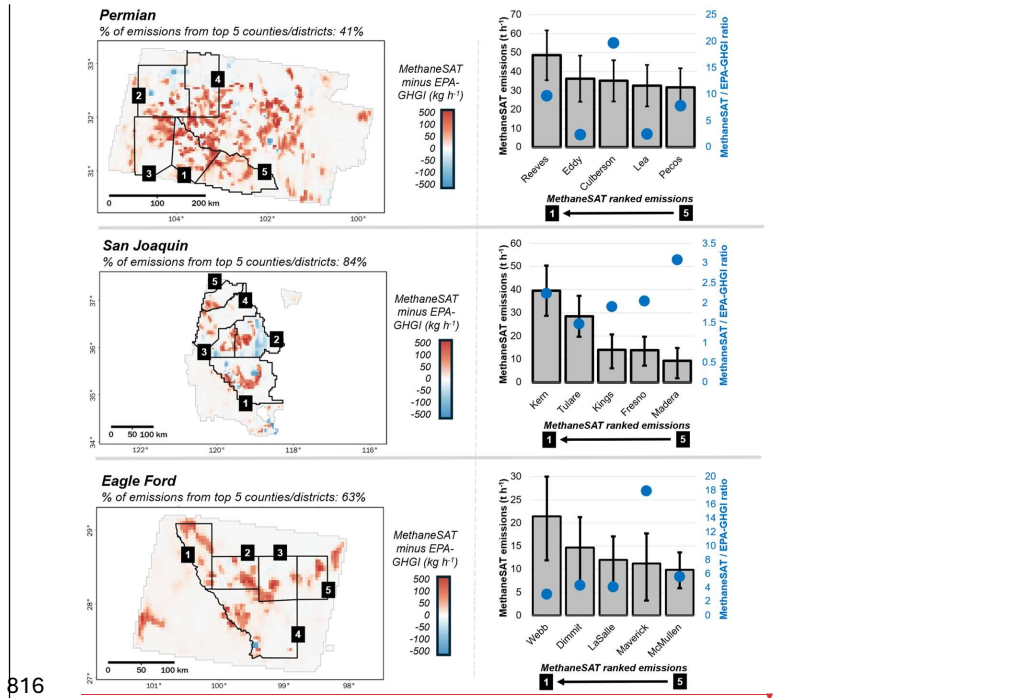


774 are consistently higher than the gridded EPA-GHGI across multiple counties/districts, with the difference driven by  
775 oil and gas emissions (Fig. 5). In Reeves County (Texas), where we observe the highest total methane emissions in  
776 the region, estimates are roughly 10-times higher than the gridded EPA-GHGI national inventory. In Eddy and Lea  
777 counties, both located in the state of New Mexico, the bottom-up inventory differences are less pronounced at a  
778 factor of two. These trends also reflect our findings of methane intensities between the states of Texas and New  
779 Mexico (Fig. 2), where intensities relative to gas and oil and gas production in Texas over twice those in New  
780 Mexico. Discrepancies between the EPA-GHGI and MethaneSAT in non-oil and gas emissions are less pronounced  
781 in the Permian, which also reflects the dominance of oil and gas emissions.

782 In the Eagle Ford region, the five highest emitting counties (i.e., Webb, Dimmit, Lasalle, Maverick, and McMullen)  
783 cumulatively account for 63% of total methane emissions within the Eagle Ford region (Fig. 5). MethaneSAT data  
784 shows consistently higher emissions compared to the EPA-GHGI in the US, and to EDGAR in Mexico (Fig. 5). The  
785 three highest emitting counties, Webb, Dimmit, and LaSalle, all have emissions estimates that are 3-4 times higher  
786 than the EPA-GHGI. By contrast, MethaneSAT emissions estimates in Maverick County are nearly 20-times higher  
787 than the EPA-GHGI, driven by differences in both oil and gas and non-oil and gas methane emissions. All three of  
788 the counties located within Mexico contain negligible emissions estimates from EDGAR. The highest emitting  
789 county we analyzed within Mexico is Sabinas County located within the Sabinas basin, Mexico's largest coal-  
790 producing region (Dávila-Pulido et al., 2023). Several distinct point sources detected by Carbon Mapper and IMEO-  
791 MARS (i.e., satellite: EMIT – NASA) attributable to coal emissions are also contained within Sabinas County (Fig.  
792 S3), with point source emission rates detected by EMIT-NASA ranging from 1.4 to 4.4  $\text{t h}^{-1}$ , and Carbon Mapper  
793 reporting a persistence-adjusted methane emission rate of 1.8  $\text{t h}^{-1}$  (95% c.i.: 1.5 – 2.1), similar to total methane  
794 emissions attributable to coal sources from MethaneSAT for this region of 1.6  $\text{t h}^{-1}$  (95% c.i.: 1.1 – 2.2).

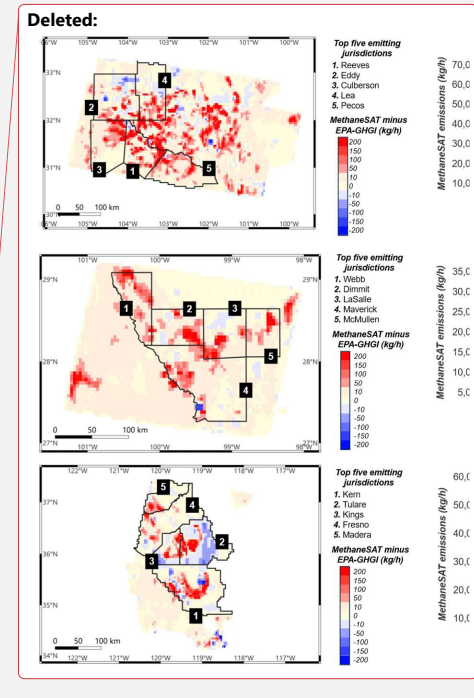
795 In the San Joaquin region, the five highest emitting counties measured by MethaneSAT (i.e., Tulare, Kings, Kern,  
796 Fresno, and Madera) account for 84% of total methane emissions within the San Joaquin region. All three counties  
797 show increased emissions relative to the EPA-GHGI by a factor of 2-3. The MethaneSAT observation domain in the  
798 San Joaquin Valley encompasses a mixture of oil and gas and non-oil and gas methane emissions sources, with  
799 predominantly non-oil and gas methane emissions focused in Kings and Tulare counties, and mixture of oil and gas,  
800 agriculture, and waste emissions in Kern County (Fig. 5). The degree of difference between the EPA-GHGI and  
801 MethaneSAT estimates in San Joaquin region is lower than the Eagle Ford or Permian, potentially due to the relative  
802 lack of oil and gas methane emissions which has been highlighted as a major sector responsible for discrepancies  
803 between top-down and bottom-up estimates in the US (Alvarez et al., 2018). The diversity in the sectoral  
804 contributions of methane emissions in the San Joaquin region is also seen in the mapping of distinct point sources  
805 from IMEO-MARS and Carbon Mapper (Fig. S3), showing two clear regions of dense point source detections  
806 related to concentrated animal feeding operations (CAFO's) in Kings and Tulare counties and point sources related  
807 to oil and gas emissions in Kern County (Fig. 5). Multiple studies have highlighted the prominence of emissions  
808 from dairy sources in Kings and Tulare counties (Cui et al., 2017; Duren et al., 2019; Heerah et al., 2021; Miller et  
809 al., 2015). Despite rising milk production in the Tulare county region, the number of dairy operations dropped since

810 the 1990's, reflecting structural changes to the dairy industry in California like the enlargement of herd sizes and  
 811 consolidation of smaller farms into larger operations (Barrowman et al., 2025). Most oil and gas emissions estimated  
 812 by MethaneSAT follow a semi-circular pattern enveloping the southeastern edge of the San Joaquin oil and gas  
 813 basin, a pattern also observed in other spatially-explicit methane emission estimates like the EI-ME and GFEI v2.  
 814 This portion of the San Joaquin oil and gas basin corresponds to a relatively dense area of oil and gas infrastructure  
 815 including refineries and processing plants.



816  
 817 **Fig. 5:** Left column displays maps showing the differences between MethaneSAT emissions estimates and the  
 818 gridded EPA-GHGI. The percentage of total MethaneSAT emissions accounted for by the top five emitting  
 819 counties/districts are indicated above each respective map. Right column displays the county/districts with the five  
 820 highest MethaneSAT emissions estimates and the respective ratios compared to the EPA-GHGI (Maasackers et al.,  
 821 2023), where a ratio of one indicates equal emissions estimates.

822  
 823 Methane emissions are evenly distributed among jurisdictions within the Amu Darya – UZB region, with the five  
 824 highest emitting counties (i.e., G'uzor, Nurobod, Usmon Yusupov, Muborak, and Buzoro) collectively emitting 34%  
 825 of emissions for the entire region (Fig. 5). Comparisons of total methane emissions estimates from MethaneSAT to  
 826 bottom-up estimates from EDGAR show variable discrepancies in emissions estimates (Fig. 5). Broadly, we find

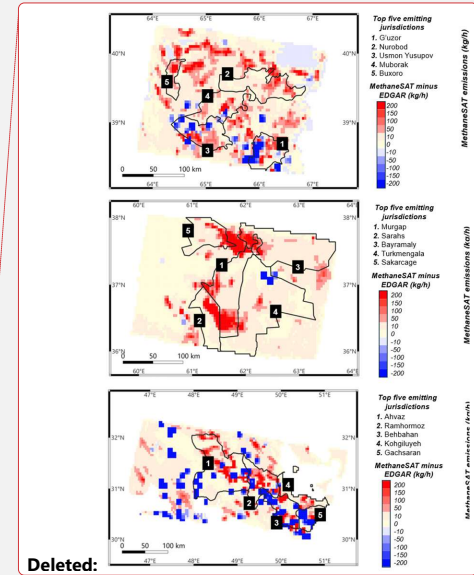
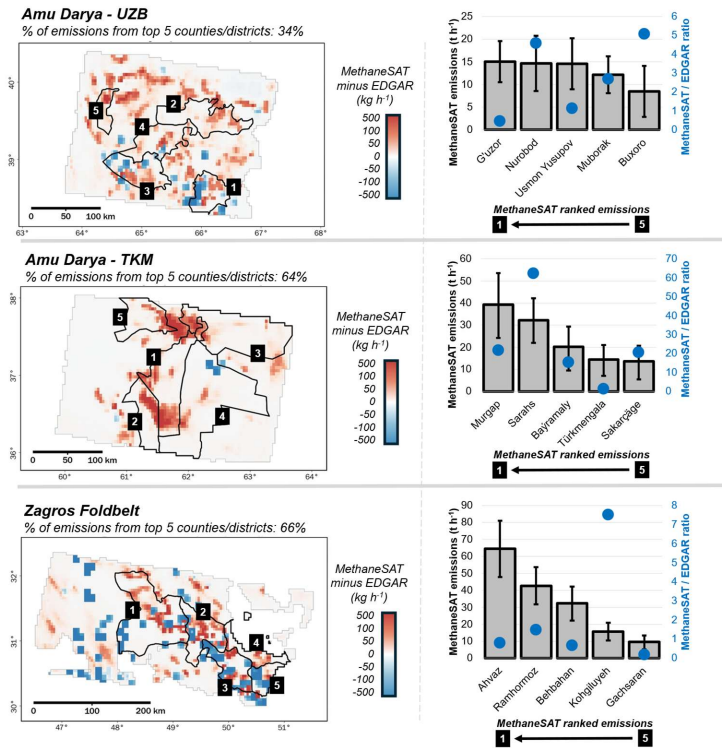


Deleted: of  
 Deleted: at the county/district level  
 Deleted: bottom-up inventories (i.e., MethaneSAT divided by  
 Deleted: The percentage of total emissions accounted for by the top five emitting counties/districts are indicated above each respective barplot.

836 that MethaneSAT estimates higher methane emissions in the North in Nurobod and Buxoro, but finds similar  
837 emissions to EDGAR in the South in G'uzor and Usmon Yusupov. The southern portion of the MethaneSAT  
838 observation domain contains most of the known oil and gas infrastructure in the region (Omara et al., 2023),  
839 including multiple distinct point source detections from IMEO-MARS and Carbon Mapper (Fig. S4). Increased  
840 methane emissions in the North are the primary explanation for why our overall estimates of methane emissions in  
841 the Amu Darya – UZB region are higher than multiple independent observations from both satellite and bottom-up  
842 inventories (Fig. 2; Fig. 3).

843 Over half (i.e., 64%) of total methane emissions in the Amu Darya – TKM region originate from the five highest  
844 emitting districts of Murgad, Sarahs, Baramaly, Turkmengala, and Sakarcage (Fig. 6). We consistently find elevated  
845 emissions estimates from MethaneSAT compared to bottom-up estimates from EDGAR (Fig. 7) to a greater degree  
846 than any of the regions we analyzed in this work. In Sarahs District which borders the city of Mary, total emissions  
847 estimates from MethaneSAT at  $32 \text{ t h}^{-1}$  are nearly 60-times higher than emissions estimates from EDGAR, due to  
848 elevated oil and gas methane emissions estimated by MethaneSAT. Across four of the five highest emitting  
849 districts/cities in the Amu Darya – TKM region, emissions estimate from MethaneSAT are a factor of 10-60 times  
850 higher than EDGAR (Fig. 7), with the exception being Turkmengala District. We also note broad discrepancies  
851 observed in the northern portion of the Amu Darya – TKM region in between Bayramaly and Sakarcage and around  
852 the city of Mary (Fig. 7). In this region, we find a high density of methane hotspots detected by TROPOMI -  
853 Sentinel-5P (Schuit et al., 2023), but a lack of point source detections from other instruments (i.e., Carbon Mapper,  
854 EMIT, PRISMA) (Fig. S4) potentially caused by limited instrument targeting in this area or by higher emissions  
855 dispersed across wider areas that may be below the detection limit of high-emitting point source detection  
856 instruments.

857 Across districts in the Zagros Foldbelt region we find consistent agreement, and even underestimation, of methane  
858 emissions from MethaneSAT compared to EDGAR (Fig. 6). [In Iran, top-down inversion studies have reported](#)  
859 [methane emissions lower than EDGAR and closer to UNFCCC inventories](#) (Maasackers et al., 2019), [with](#)  
860 [discrepancies likely arising in part from differences in the representation of oil and gas emissions and EDGAR's use](#)  
861 [of generalized emission factors](#) (Crippa et al., 2024). Cumulatively, the top five highest emitting districts (Ahvaz,  
862 Ramhormoz, Behbahan, Kohgiluyeh, and Gachsaran) are responsible for 66% of total methane emissions in the  
863 Zagros Foldbelt region. Except for Kohgiluyeh, MethaneSAT emissions estimates for all these jurisdictions are  
864 within a factor of 2 compared to EDGAR. Residual emissions in the region show neighboring positive and negative  
865 values, especially for oil and gas emissions following the NE-SW domain of the Zagros Foldbelt basin (Fig. 7).



866

867 **Fig. 6:** Left column displays maps showing the differences between MethaneSAT emissions estimates and the  
 868 EDGAR\_2025\_GHG bottom-up methane inventory. The percentage of total MethaneSAT emissions accounted for  
 869 by the top five emitting counties/districts are indicated above each respective map. Right column displays the  
 870 jurisdictions with the five highest MethaneSAT emissions estimates and the respective ratios compared to EDGAR  
 871 (i.e., EDGAR 2025\_GHG) (Crippa et al., 2024), where a ratio of one indicates equal emissions estimates.

872

873

874

875 **4 Discussion**

876 We demonstrate MethaneSAT's ability to deliver satellite-based quantification of methane emissions across six  
 877 major oil and gas producing regions, leveraging its high precision, high-resolution observations and wide mapping  
 878 domains (~220 - 440 km swaths). These capabilities enable measurement-based constraints that complement  
 879 bottom-up inventories, reveal spatial emission patterns and potential new hotspots, and support targeted mitigation

**Deleted:** across jurisdictions (i.e., counties, districts)

**Deleted:** bottom-up inventories (i.e., MethaneSAT divided by the

**Deleted:** . The percentage of total emissions accounted for by the top five emitting counties/districts are indicated above each respective barplot.

**Deleted:** We provide new satellite-based quantification of methane emissions across six major oil and gas producing regions derived using MethaneSAT's high precision, high-resolution observations combined with its wide mapping domains

892 [strategies](#) (Jacob et al., 2022; Saunio et al., 2025; Shen et al., 2023). [The value of this observing system is](#)  
893 [particularly evident in the Amu Darya – TKM region, where our analysis reveals 5-8 times higher emissions relative](#)  
894 [to existing bottom-up inventories for the full observation domain \(Fig. 4\), and 15–62 times higher across four of the](#)  
895 top five emitting jurisdictions (Fig. 6). These results not only underscore the importance of updated, measurement-  
896 based assessments for the Amu Darya basin in Turkmenistan, but the value of high-resolution methane emissions  
897 maps that can highlight specific jurisdictions responsible for the underestimation of methane emissions in bottom-up  
898 inventories, which are important for accounting and mitigation of methane emissions.

**Deleted:** Satellite observations offer measurement-based constraints that complement bottom-up inventories, reveal spatial emission patterns and potential new hot spots, and support targeted mitigation strategies

899 [Importantly, bottom-up inventories and methane emissions data from MethaneSAT differ in their temporal](#)  
900 representation (i.e., annual estimates versus an aggregation of multiple satellite overpasses). However, we can infer  
901 insights into the spatial distribution of emissions across jurisdictions and identify subregions where inventories  
902 potentially under- or over-estimate emissions. In the US, we compare MethaneSAT emissions estimates to 2020  
903 annual estimates from the EPA-GHGI and find consistent underestimation in the national inventory across multiple  
904 counties/districts (Fig. 5), with the highest emissions in Reeves County (US, Texas) at  $49 \text{ t h}^{-1}$  which are a factor of  
905  $\sim 10$  higher than the EPA-GHGI. We also find, in the Permian basin, that counties in New Mexico have more  
906 comparable emissions to the EPA-GHGI compared to those in Texas. [Top-down/bottom-up discrepancies are well-](#)

**Deleted:** We investigate emissions estimates at county/district-level scales to identify the highest emitting subregions and localize areas of discrepancies compared to bottom-up inventories.

907 [documented in the US literature \(Alvarez et al., 2018; MacKay et al., 2025; Shen et al., 2022\) and refined](#)  
908 [inventories like the VISTA-CA for the San Joaquin dairy sector \(Marklein et al., 2021; Schulze et al., 2023\) and EI-](#)  
909 [ME for the oil and gas sector \(Omara et al., 2024\) demonstrate that such gaps are closeable.](#) Outside of the US, we  
910 observe the highest emissions in Ahvaz District (Iran) at  $82 \text{ t h}^{-1}$ , but find comparable emissions estimates to  
911 EDGAR (Fig. 4, Fig. 6). Other broader insights include the relative contribution of emissions from jurisdictionally  
912 boundaries to larger regional estimates. For example, in the Permian and Amu Darya - UZB regions, the  
913 contribution from the top five districts/counties (i.e., 41% and 34% respectively) indicate a greater spread of  
914 emissions across the entire measurement domains. In the San Joaquin, Zagros Foldbelt, and Amu Darya - TKM  
915 regions we find higher contributions from the top five emitting jurisdictions at 84%, 66%, and 64% respectively,  
916 which indicates that emissions are more localized. A key factor to consider when quantifying emissions for these  
917 smaller regions is the growth in uncertainty as the spatial domain of interest becomes smaller, [and single grid-cell](#)  
918 [estimates \( \$0.04^\circ \times 0.04^\circ\$ \) from MethaneSAT carry substantial uncertainty.](#) Repeated observations can help reduce

**Deleted:** Discrepancies between bottom-up estimates and top-down inversions are consistently observed in the US, further supporting refinements to bottom-up emissions estimates where agreement between bottom-up and top-down can improve. There are several examples of refined bottom-up inventories in the US, including the VISTA-CA dairy emissions inventory in the San Joaquin region where Schulze et al. found greater agreement compared to independent mass-balance flights, or the EI-ME oil and gas emissions inventory presented in Omara et al. where national oil and gas emissions estimates were in wide agreement with multiple satellite-based estimates.

919 this uncertainty and identify more robust trends over space and time, [and emission estimates for larger subregions](#)  
920 with multiple observations will inherently be more robust due to the aggregation of data and partial cancellation of  
921 random errors, increasing the statistical confidence in any conclusions derived from the data. MethaneSAT does not  
922 incorporate a bottom-up prior emissions inventory to inform the spatial allocation of methane emissions and  
923 therefore it relies on the high-precision measurement aspects of the input XCH<sub>4</sub> data which resolves methane  
924 concentration gradients at high precision (2.5 – 5.5 ppb at 2 km x 2 km resolution) (Chan Miller et al., 2024).

**Deleted:** In the context of MethaneSAT, this effect is most pronounced when analyzing emissions from single  $0.04^\circ \times 0.04^\circ$  emission rate estimates (i.e., a single grid cell).

925 [Sectoral attribution is applied as a post-inversion step using a composite prior inventory drawn from multiple](#)  
926 [spatially explicit datasets supplemented by global point source data from Carbon Mapper \(2025\). This approach](#)  
927 [improves sectoral allocation,](#) especially for regions where information on oil and gas emissions data is sparse and  
928 information from one inventory can account for discrepancies in another (SI – Section 1.1, Fig. S5). Most of our

**Deleted:** but conclusions derived from a single observation grid from MethaneSAT should be subject to large uncertainty.

**Deleted:** In the post analysis of MethaneSAT data, we utilize a composite prior emissions inventory for the sectoral allocation of methane emissions based on sector-specific estimates from multiple spatially explicit datasets including global point source data from Carbon Mapper to create a more comprehensive and spatially resolved dataset. We use this approach to improve the sectoral allocation of methane emissions by sector after the flux inversion process,

**Deleted:** An additional characteristic from sectoral emissions estimates from MethaneSAT, are relatively high methane emissions associated with non-oil and gas emissions compared to other spatially-explicit inventories (Fig. 3) which we also observe in other satellite-based datasets such as Varon et al. in our Permian methane emissions estimates.

969 sectoral-attributed non-oil and gas emission estimates from MethaneSAT originate from agricultural sources (Fig. 3),  
970 a pattern also observed in more recent TROPOMI-based estimates for regions like the Permian, Amu Darya – TKM,  
971 and Amu Darya - UZB (East et al., 2025; Varon et al., 2025), which reflects agricultural emissions within prior  
972 inventories that cover much larger areas than the localized oil and gas emissions within the same inventories.  
973 Artifacts from the MethaneSAT inversion process arising from wind errors coupled with a non-negativity of  
974 emissions quantification may be expected to result in small contributions (i.e., <15%) of diffuse emissions  
975 throughout the scenes (Fig. S11), which are predominantly allocated to agricultural sources in the absence of others.  
976 Together, these characteristics suggest that MethaneSAT's non-oil and gas emission estimates should be interpreted  
977 with caution, as they may partly reflect methodological features of fine-resolution inversion rather than true  
978 emission signals.

979 Oil and gas intensity metrics, both normalized by marketed gas production (i.e., loss rates) and combined oil and gas  
980 production (i.e., energy intensity), function as a performance standard for oil and gas operators and highlight the  
981 cost-effectiveness of mitigation from the oil and gas sector (Overview – Global Methane Tracker 2022 – Analysis,  
982 2025). We find elevated loss rates in both the San Joaquin and Zagros Foldbelt basins relative to the other regions  
983 we analyzed in this work. Both the San Joaquin and Zagros Foldbelt basins are primarily oil-producing and  
984 characterized by a long legacy of oil and gas development, with aging and potentially inefficient infrastructure that  
985 may be leading to the high loss rates. In contrast, the Eagle Ford basin has the lowest loss rate and is the youngest oil  
986 and gas basin among the regions we cover. All of the oil and gas basins studied in this work have loss rates well  
987 above the 0.2% methane intensity target set by the oil and gas decarbonization charter to reduce industry's emissions  
988 by year 2030 (Oil and Gas Climate Initiative | OGCI, 2025), noting that operators within Turkmenistan, Uzbekistan,  
989 and Iran are not participants in this coalition. At a finer-scale than basin-wide estimates, the high-resolution methane  
990 emissions heatmaps from MethaneSAT highlight significant interstate differences in the Permian basin with loss  
991 rates observed across the New Mexico and Texas state boundaries of the Delaware subbasin at 1.3% and 3.1%  
992 respectively, a finding also observed in TROPOMI-based inversions from 2019-2023 (Varon et al., 2025), and  
993 coincide with stronger emission controls introduced in New Mexico relative to Texas (EDF Data Story, 2025). While  
994 beyond the scope of this work and subject to associated uncertainties, MethaneSAT emissions maps can be used to  
995 derive methane intensities across individual jurisdictions, noting that a key limiting factor would be the granularity  
996 of oil and gas production data, especially for regions outside of the US. Even in the US, the heterogeneity and  
997 comingling of oil and gas operators prevents specific operator attribution from MethaneSAT observations, except for  
998 point source detections (Guanter et al., 2026), which are not included in this work. Our results demonstrate basin,  
999 sub-basin and individual jurisdictional-scale emission insights derived using the relatively short operational lifetime  
1000 of MethaneSAT towards advancing the state of emission quantification to further support and motivate methane  
1001 mitigation action from the oil and gas sector.

## 1003 5 Conclusions

**Deleted:** energy

**Deleted:** These findings of lower loss rates in the New Mexico portion of the Delaware sub-basin of Permian coincide with stronger emission controls introduced in New Mexico relative to Texas.

**Deleted:** (Guanter et al., 2025)

**Deleted:** Internationally, many countries are dominated by state-owned oil and gas operations where attribution to oil and gas producers is more straightforward.

**Deleted:** Nevertheless, these results demonstrate basin, sub-basin and individual jurisdictional-scale emission insights derived using the relatively short operational lifetime of MethaneSAT towards advancing the state of emission quantification in order to further support and motivate methane mitigation action from the oil and gas sector.

1019 The results we present here are a summary of insights from six diverse oil and gas producing regions around the  
1020 world, demonstrating the capabilities of MethaneSAT. Among our results, the statistically robust methane emissions  
1021 quantifications across jurisdictional bounds is perhaps the most influential for supporting countries/industries/cities  
1022 to monitor and mitigate methane emissions. Fine-scale methane emissions data illuminate specific areas of  
1023 discrepancies from bottom-up inventories which are commonly used to inform methane mitigation policy - all  
1024 through atmospheric observations. A notable example is the Amu Darya -TKM region, where MethaneSAT  
1025 estimates are nearly 10-times higher than bottom-up estimates from CAMS v6.2 and EDGAR. Other broader  
1026 insights include the consistent discrepancy with the EPA-GHGI from our MethaneSAT emissions estimates in the  
1027 US, loss rates exceeding 10% in the oil-dominant basins of San Joaquin and Zagros Foldbelt and energy intensities  
1028 exceeding 0.40 kg CH<sub>4</sub> GJ<sup>-1</sup> in Amu Darya UZB/TKM and San Joaquin regions. Many capabilities of MethaneSAT  
1029 are demonstrated in this work, and future improvements to data acquired and processed over the lifetime of the  
1030 satellite will continue to be refined and released in the public domain to help further improve the understanding and  
1031 mitigation potential of methane emissions at multiple scales, especially for the oil and gas sector.

1032  
1033  
1034

1035 **Data availability:** MethaneSAT data products are publicly accessible through Google Earth Engine: L3  
1036 concentration maps, L4 area emissions. The Level-1B onwards data products are additionally available via the  
1037 public request (link).

1038 **Supplement link:** The supplement is available for download online

1039 **Author contribution:** JPW and RG conceived the study. Funding acquisition was led by RG, SCW, and SPH. Data  
1040 collection and field measurements were conducted by JPW, JB, MK, MO, AH, KW, BL, JW, and KM. Science  
1041 algorithms, data processing and software development were performed by JB, MK, EK, SA, MR, NL, TM, CCM,  
1042 SR, MS, JF, BL, and DM. Formal data analysis was carried out by JPW, MO, AH, KW, BL, MK, JB, SCW and RG.  
1043 Visualization and figure preparation were led by JPW, with contributions from MO, AH, KW, and BL. Methodology  
1044 development was conducted by JPW, JB, MK, SA, MR, NL, TM, CCM, and SR. Project supervision was provided  
1045 by RG. JPW wrote the original draft of the manuscript. Writing, review, and editing were contributed by RG, MO,  
1046 EK, DM, MK, KM, and LG.

1047 **Financial support:** Funding for MethaneSAT activities was provided in part by anonymous donors, Arnold  
1048 Ventures, The Audacious Project, the Ballmer Group, the Bezos Earth Fund, The Children's Investment Fund  
1049 Foundation, the Heising-Simons Family Fund, King Philanthropies, the Robertson Foundation, the Skyline  
1050 Foundation, and the Valhalla Foundation. For a more complete list of funders, please visit  
1051 <https://www.methanesat.org/> (last access: 8 December 2025).

1052 **Competing interests:** The authors declare no competing interests.

**Deleted:** with any single region deserving of more focused analysis

**Deleted:** are

**Deleted:** key

**Deleted:** we show

**Deleted:** found in

**Deleted:** of Turkmenistan

**Deleted:** further investigation could shed more light to the specific sectors and sources of the large discrepancies we find

**Deleted:** as well as gas-production normalized

**Deleted:** which are both characterized by legacy oil and gas producing infrastructure

**Deleted:** in particular across

**Deleted:** Appendix A: Description of MethaneSAT emissions inversion process¶  
Appendix B: Uncertainty calculations¶

**Deleted:** Composite emissions maps are available for download at Zenodo (link: xxxx), with associated links to the individual MethaneSAT scenes listed and publicly available through Google Earth Engine, and data used to reproduce the figures in the main text. Code used to produce emission map aggregation and sectoral disaggregation are available upon reasonable request.

**Deleted:** to this preprint

- 1078
- 1079
- 1080 **4. References**
- 1081 Alipour, M.: Petroleum systems of the Iranian Zagros Fold and Thrust Belt, *Results in Earth Sciences*, 2, 100027,  
1082 <https://doi.org/10.1016/j.rines.2024.100027>, 2024.
- 1083 Alvarez, R. A., Zavala-Araiza, D., Lyon, D. R., Allen, D. T., Barkley, Z. R., Brandt, A. R., Davis, K. J., Herndon, S.  
1084 C., Jacob, D. J., Karion, A., Kort, E. A., Lamb, B. K., Lauvaux, T., Maasakkers, J. D., Marchese, A. J., Omara, M.,  
1085 Pacala, S. W., Peischl, J., Robinson, A. L., Shepson, P. B., Sweeney, C., Townsend-Small, A., Wofsy, S. C., and  
1086 Hamburg, S. P.: Assessment of methane emissions from the U.S. oil and gas supply chain, *Science*, 361, 186–188,  
1087 <https://doi.org/10.1126/science.aar7204>, 2018.
- 1088 Wood Mackenzie: <https://www.woodmac.com/lens>, last access: 19 November 2025.
- 1089 Dashboard | Carbon Mapper: <https://data.carbonmapper.org/#1.3/30.8/50.5>, last access: 3 December 2025.
- 1090 EDF Data Story: <https://www.edf.org/methanesat-observations-reveal-lower-methane-intensity-new-mexico-permian-basin-associated>, last access: 5 December 2025.
- 1091
- 1092 IEA: <https://www.iea.org/countries/iraq>, last access: 30 September 2025.
- 1093 N.M. Code R. § 19.15.27.9 Statewide Natural Gas Capture Requirements: <https://regulations.vlex.com/vid/n-m-code-r-955851862>, last access: 3 September 2025.
- 1094
- 1095 NOAA Institutional Repository: <https://repository.library.noaa.gov>, last access: 16 March 2026.
- 1096 OGDC - The Charter: <https://www.ogdc.org/>, last access: 5 December 2025.
- 1097 Oil and Gas Climate Initiative | OGCI: <https://www.ogci.com/>, last access: 30 September 2025.
- 1098 Overview – Global Methane Tracker 2022 – Analysis: <http://www.iea.org/reports/global-methane-tracker-2022/overview>, last access: 30 September 2025.
- 1099
- 1100 PermianMAP: <https://data.permianmap.org/pages/operators>, last access: 1 September 2025.
- 1101 UNFCCC: [https://di.unfccc.int/detailed\\_data\\_by\\_party](https://di.unfccc.int/detailed_data_by_party), last access: 3 September 2025.
- 1102 Uzbekistan - Countries & Regions: <https://www.iea.org/countries/uzbekistan/oil>, last access: 30 September 2025.
- 1103 Barkley, Z., Davis, K., Miles, N., Richardson, S., Deng, A., Hmiel, B., Lyon, D., and Lauvaux, T.: Quantification of  
1104 oil and gas methane emissions in the Delaware and Marcellus basins using a network of continuous tower-based  
1105 measurements, *Atmospheric Chemistry and Physics*, 23, 6127–6144, <https://doi.org/10.5194/acp-23-6127-2023>,  
1106 2023.
- 1107 Barrowman, S., Yurco, K., Sumner, D., and Cooper, M. H.: MORE MILK, FEWER FARMS, and REGIONAL  
1108 CONCENTRATION: MAPPING TRANSFORMATIONS IN CALIFORNIA'S DAIRY INDUSTRY, *Geographical*  
1109 *Review*, 115, 49–80, <https://doi.org/10.1080/00167428.2024.2391832>, 2025.
- 1110 Bloom, A. A., Bowman, K. W., Lee, M., Turner, A. J., Schroeder, R., Worden, J. R., Weidner, R., McDonald, K. C.,  
1111 and Jacob, D. J.: A global wetland methane emissions and uncertainty dataset for atmospheric chemical transport  
1112 models (WetCHARTs version 1.0), *Geoscientific Model Development*, 10, 2141–2156, <https://doi.org/10.5194/gmd-10-2141-2017>, 2017.  
1113

- 1114 Burdeau, P. M., Sherwin, E. D., Biraud, S. C., Berman, E. S. F., and Brandt, A. R.: High-resolution national mapping  
 1115 of natural gas composition substantially updates methane leakage impacts, *Nat Commun*, 16, 11297,  
 1116 <https://doi.org/10.1038/s41467-025-66465-6>, 2025.
- 1117 Carpenter, B., Gelman, A., Hoffman, M. D., Lee, D., Goodrich, B., Betancourt, M., Brubaker, M., Guo, J., Li, P., and  
 1118 Riddell, A.: Stan: A Probabilistic Programming Language, *Journal of Statistical Software*, 76, 1–32,  
 1119 <https://doi.org/10.18637/jss.v076.i01>, 2017.
- 1120 Chan Miller, C., Roche, S., Wilzewski, J. S., Liu, X., Chance, K., Souri, A. H., Conway, E., Luo, B., Samra, J.,  
 1121 Hawthorne, J., Sun, K., Staebell, C., Chulakadabba, A., Sargent, M., Benmergui, J. S., Franklin, J. E., Daube, B. C.,  
 1122 Li, Y., Laughner, J. L., Baier, B. C., Gautam, R., Omara, M., and Wofsy, S. C.: Methane retrieval from MethaneAIR  
 1123 using the CO<sub>2</sub> proxy approach: a demonstration for the upcoming MethaneSAT mission, *Atmospheric Measurement  
 1124 Techniques*, 17, 5429–5454, <https://doi.org/10.5194/amt-17-5429-2024>, 2024.
- 1125 Chen, Y., Sherwin, E. D., Berman, E. S. F., Jones, B. B., Gordon, M. P., Wetherley, E. B., Kort, E. A., and Brandt, A.  
 1126 R.: Quantifying Regional Methane Emissions in the New Mexico Permian Basin with a Comprehensive Aerial  
 1127 Survey, *Environ. Sci. Technol.*, 56, 4317–4323, <https://doi.org/10.1021/acs.est.1c06458>, 2022.
- 1128 Chen, Z., Jacob, D. J., Gautam, R., Omara, M., Stavins, R. N., Stowe, R. C., Nesser, H., Sulprizio, M. P., Lorente,  
 1129 A., Varon, D. J., Lu, X., Shen, L., Qu, Z., Pendergrass, D. C., and Hancock, S.: Satellite quantification of methane  
 1130 emissions and oil–gas methane intensities from individual countries in the Middle East and North Africa:  
 1131 implications for climate action, *Atmospheric Chemistry and Physics*, 23, 5945–5967, <https://doi.org/10.5194/acp-23-5945-2023>, 2023.
- 1133 Crippa, M., Guizzardi, D., Pagani, F., Schiavina, M., Melchiorri, M., Pisoni, E., Graziosi, F., Muntean, M., Maes, J.,  
 1134 Dijkstra, L., Van Damme, M., Clarisse, L., and Coheur, P.: Insights into the spatial distribution of global, national,  
 1135 and subnational greenhouse gas emissions in the Emissions Database for Global Atmospheric Research (EDGAR  
 1136 v8.0), *Earth System Science Data*, 16, 2811–2830, <https://doi.org/10.5194/essd-16-2811-2024>, 2024.
- 1137 Cui, Y. Y., Brioude, J., Angevine, W. M., Peischl, J., McKeen, S. A., Kim, S.-W., Neuman, J. A., Henze, D. K.,  
 1138 Bousserez, N., Fischer, M. L., Jeong, S., Michelsen, H. A., Bambha, R. P., Liu, Z., Santoni, G. W., Daube, B. C.,  
 1139 Kort, E. A., Frost, G. J., Ryerson, T. B., Wofsy, S. C., and Trainer, M.: Top-down estimate of methane emissions in  
 1140 California using a mesoscale inverse modeling technique: The San Joaquin Valley, *Journal of Geophysical Research:  
 1141 Atmospheres*, 122, 3686–3699, <https://doi.org/10.1002/2016JD026398>, 2017.
- 1142 Cusworth, D. H., Bloom, A. A., Ma, S., Miller, C. E., Bowman, K., Yin, Y., Maasakkers, J. D., Zhang, Y., Scarpelli,  
 1143 T. R., Qu, Z., Jacob, D. J., and Worden, J. R.: A Bayesian framework for deriving sector-based methane emissions  
 1144 from top-down fluxes, *Commun Earth Environ*, 2, 242, <https://doi.org/10.1038/s43247-021-00312-6>, 2021a.
- 1145 Cusworth, D. H., Duren, R. M., Thorpe, A. K., Olson-Duvall, W., Heckler, J., Chapman, J. W., Eastwood, M. L.,  
 1146 Helmlinger, M. C., Green, R. O., Asner, G. P., Dennison, P. E., and Miller, C. E.: Intermittency of Large Methane  
 1147 Emitters in the Permian Basin, *Environ. Sci. Technol. Lett.*, 8, 567–573, <https://doi.org/10.1021/acs.estlett.1c00173>,  
 1148 2021b.
- 1149 Cusworth, D. H., Thorpe, A. K., Ayasse, A. K., Stepp, D., Heckler, J., Asner, G. P., Miller, C. E., Yadav, V.,  
 1150 Chapman, J. W., Eastwood, M. L., Green, R. O., Hmiel, B., Lyon, D. R., and Duren, R. M.: Strong methane point  
 1151 sources contribute a disproportionate fraction of total emissions across multiple basins in the United States,  
 1152 *Proceedings of the National Academy of Sciences*, 119, e2202338119, <https://doi.org/10.1073/pnas.2202338119>,  
 1153 2022.
- 1154 Dávila-Pulido, G. I., González-Ibarra, A. A., and Garza-García, M.: A brief review on coal reserves, production and  
 1155 possible non-power uses: The case of Mexico, *Heliyon*, 9, <https://doi.org/10.1016/j.heliyon.2023.e16043>, 2023.
- 1156 Duren, R., Cusworth, D., Ayasse, A., Howell, K., Diamond, A., Scarpelli, T., Kim, J., O’neill, K., Lai-Norling, J.,  
 1157 Thorpe, A., Zandbergen, S. R., Shaw, L., Keremedjiev, M., Guido, J., Giuliano, P., Goldstein, M., Nallapu, R.,

1158 Barentsen, G., Thompson, D. R., Roth, K., Jensen, D., Eastwood, M., Reuland, F., Adams, T., Brandt, A., Kort, E.  
1159 A., Mason, J., and Green, R. O.: The Carbon Mapper emissions monitoring system, *Atmospheric Measurement*  
1160 *Techniques*, 18, 6933–6958, <https://doi.org/10.5194/amt-18-6933-2025>, 2025.

1161 Duren, R. M., Thorpe, A. K., Foster, K. T., Rafiq, T., Hopkins, F. M., Yadav, V., Bue, B. D., Thompson, D. R.,  
1162 Conley, S., Colombi, N. K., Frankenberg, C., McCubbin, I. B., Eastwood, M. L., Falk, M., Herner, J. D., Croes, B.  
1163 E., Green, R. O., and Miller, C. E.: California’s methane super-emitters, *Nature*, 575, 180–184,  
1164 <https://doi.org/10.1038/s41586-019-1720-3>, 2019.

1165 East, J. D., Jacob, D. J., Jervis, D., Balasus, N., Estrada, L. A., Hancock, S. E., Sulprizio, M. P., Thomas, J., Wang,  
1166 X., Chen, Z., Varon, D. J., and Worden, J. R.: Worldwide inference of national methane emissions by inversion of  
1167 satellite observations with UNFCCC prior estimates, *Nat Commun*, 16, 11004, [https://doi.org/10.1038/s41467-025-](https://doi.org/10.1038/s41467-025-67122-8)  
1168 [67122-8](https://doi.org/10.1038/s41467-025-67122-8), 2025.

1169 Fasoli, B., Lin, J. C., Bowling, D. R., Mitchell, L., and Mendoza, D.: Simulating atmospheric tracer concentrations  
1170 for spatially distributed receptors: updates to the Stochastic Time-Inverted Lagrangian Transport model’s R interface  
1171 (STILT-R version 2), *Geoscientific Model Development*, 11, 2813–2824, [https://doi.org/10.5194/gmd-11-2813-](https://doi.org/10.5194/gmd-11-2813-2018)  
1172 [2018](https://doi.org/10.5194/gmd-11-2813-2018), 2018.

1173 Fung, I., John, J., Lerner, J., Matthews, E., Prather, M., Steele, L. P., and Fraser, P. J.: Three-dimensional model  
1174 synthesis of the global methane cycle, *Journal of Geophysical Research: Atmospheres*, 96, 13033–13065,  
1175 <https://doi.org/10.1029/91JD01247>, 1991.

1176 Granier, C., Darras, S., Denier van Der Gon, H., Jana, D., Elguindi, N., Bo, G., Michael, G., Marc, G., Jalkanen, J.-  
1177 P., Kuenen, J., Lioussé, C., Quack, B., Simpson, D., and Sindelarova, K.: The Copernicus Atmosphere Monitoring  
1178 Service global and regional emissions (April 2019 version), Copernicus Atmosphere Monitoring Service,  
1179 <https://doi.org/10.24380/d0bn-kx16>, 2019.

1180 Guanter, L., Roger, J., Warren, J., Sargent, M., Zhang, Z., Roche, S., Miller, C. C., Steiner, M., Hadfield, H., Omara,  
1181 M., Williams, J., MacKay, K., Franklin, J. E., Luo, B., Wofsy, S. C., Hamburg, S. P., and Gautam, R.: Surveying  
1182 methane point-source super-emissions across oil and gas basins with MethaneSAT, *Atmospheric Chemistry and*  
1183 *Physics*, 26, 2941–2963, <https://doi.org/10.5194/acp-26-2941-2026>, 2026.

1184 Heerah, S., Frausto-Vicencio, I., Jeong, S., Marklein, A. R., Ding, Y., Meyer, A. G., Parker, H. A., Fischer, M. L.,  
1185 Franklin, J. E., Hopkins, F. M., and Dubey, M.: Dairy Methane Emissions in California’s San Joaquin Valley  
1186 Inferred With Ground-Based Remote Sensing Observations in the Summer and Winter, *Journal of Geophysical*  
1187 *Research: Atmospheres*, 126, e2021JD034785, <https://doi.org/10.1029/2021JD034785>, 2021.

1188 Hmiel, B., Lyon, D. R., Warren, J. D., Yu, J., Cusworth, D. H., Duren, R. M., and Hamburg, S. P.: Empirical  
1189 quantification of methane emission intensity from oil and gas producers in the Permian basin, *Environ. Res. Lett.*,  
1190 18, 024029, <https://doi.org/10.1088/1748-9326/acb27e>, 2023.

1191 Hoffman, M. D. and Gelman, A.: The No-U-Turn Sampler: Adaptively Setting Path Lengths in Hamiltonian Monte  
1192 Carlo, <https://doi.org/10.48550/arXiv.1111.4246>, 18 November 2011.

1193 Irakulis-Loitxate, I., Guanter, L., Liu, Y.-N., Varon, D. J., Maasakkers, J. D., Zhang, Y., Chulakadabba, A., Wofsy, S.  
1194 C., Thorpe, A. K., Duren, R. M., Frankenberg, C., Lyon, D. R., Hmiel, B., Cusworth, D. H., Zhang, Y., Segl, K.,  
1195 Gorroño, J., Sánchez-García, E., Sulprizio, M. P., Cao, K., Zhu, H., Liang, J., Li, X., Aben, I., and Jacob, D. J.:  
1196 Satellite-based survey of extreme methane emissions in the Permian basin, *Science Advances*, 7, eabf4507,  
1197 <https://doi.org/10.1126/sciadv.abf4507>, 2021.

1198 Jacob, D. J., Varon, D. J., Cusworth, D. H., Dennison, P. E., Frankenberg, C., Gautam, R., Guanter, L., Kelley, J.,  
1199 McKeever, J., Ott, L. E., Poulter, B., Qu, Z., Thorpe, A. K., Worden, J. R., and Duren, R. M.: Quantifying methane  
1200 emissions from the global scale down to point sources using satellite observations of atmospheric methane,  
1201 *Atmospheric Chemistry and Physics*, 22, 9617–9646, <https://doi.org/10.5194/acp-22-9617-2022>, 2022.

- 1202 Jervis, D., McKeever, J., Durak, B. O. A., Sloan, J. J., Gains, D., Varon, D. J., Ramier, A., Strupler, M., and Tarrant,  
1203 E.: The GHGSat-D imaging spectrometer, *Atmospheric Measurement Techniques*, 14, 2127–2140,  
1204 <https://doi.org/10.5194/amt-14-2127-2021>, 2021.
- 1205 Johnson, M. R., Conrad, B. M., Zimmerle, D. J., and Kleinberg, R. L.: Methane by the Numbers: The Need for Clear  
1206 and Comparable Methane Intensity Metrics, *Environ. Sci. Technol.*, <https://doi.org/10.1021/acs.est.5c13990>, 2026.
- 1207 Lin, J. C., Gerbig, C., Wofsy, S. C., Andrews, A. E., Daube, B. C., Davis, K. J., and Grainger, C. A.: A near-field tool  
1208 for simulating the upstream influence of atmospheric observations: The Stochastic Time-Inverted Lagrangian  
1209 Transport (STILT) model, *Journal of Geophysical Research: Atmospheres*, 108,  
1210 <https://doi.org/10.1029/2002JD003161>, 2003.
- 1211 Lu, X., Jacob, D. J., Zhang, Y., Maasakkers, J. D., Sulprizio, M. P., Shen, L., Qu, Z., Scarpelli, T. R., Nesser, H.,  
1212 Yantosca, R. M., Sheng, J., Andrews, A., Parker, R. J., Boesch, H., Bloom, A. A., and Ma, S.: Global methane  
1213 budget and trend, 2010–2017: complementarity of inverse analyses using in situ (GLOBALVIEWplus CH<sub>4</sub>  
1214 ObsPack) and satellite (GOSAT) observations, *Atmospheric Chemistry and Physics*, 21, 4637–4657,  
1215 <https://doi.org/10.5194/acp-21-4637-2021>, 2021.
- 1216 Lu, X., Jacob, D. J., Wang, H., Maasakkers, J. D., Zhang, Y., Scarpelli, T. R., Shen, L., Qu, Z., Sulprizio, M. P.,  
1217 Nesser, H., Bloom, A. A., Ma, S., Worden, J. R., Fan, S., Parker, R. J., Boesch, H., Gautam, R., Gordon, D., Moran,  
1218 M. D., Reuland, F., Villasana, C. A. O., and Andrews, A.: Methane emissions in the United States, Canada, and  
1219 Mexico: evaluation of national methane emission inventories and 2010–2017 sectoral trends by inverse analysis of  
1220 in situ (GLOBALVIEWplus CH<sub>4</sub> ObsPack) and satellite (GOSAT) atmospheric observations, *Atmospheric  
1221 Chemistry and Physics*, 22, 395–418, <https://doi.org/10.5194/acp-22-395-2022>, 2022.
- 1222 Lu, X., Jacob, D. J., Zhang, Y., Shen, L., Sulprizio, M. P., Maasakkers, J. D., Varon, D. J., Qu, Z., Chen, Z., Hmiel,  
1223 B., Parker, R. J., Boesch, H., Wang, H., He, C., and Fan, S.: Observation-derived 2010–2019 trends in methane  
1224 emissions and intensities from US oil and gas fields tied to activity metrics, *Proceedings of the National Academy of  
1225 Sciences*, 120, e2217900120, <https://doi.org/10.1073/pnas.2217900120>, 2023.
- 1226 Maasakkers, J. D., Jacob, D. J., Sulprizio, M. P., Scarpelli, T. R., Nesser, H., Sheng, J.-X., Zhang, Y., Hersher, M.,  
1227 Bloom, A. A., Bowman, K. W., Worden, J. R., Janssens-Maenhout, G., and Parker, R. J.: Global distribution of  
1228 methane emissions, emission trends, and OH concentrations and trends inferred from an inversion of GOSAT  
1229 satellite data for 2010–2015, *Atmospheric Chemistry and Physics*, 19, 7859–7881, <https://doi.org/10.5194/acp-19-7859-2019>, 2019.
- 1231 Maasakkers, J. D., McDuffie, E. E., Sulprizio, M. P., Chen, C., Schultz, M., Brunelle, L., Thrush, R., Steller, J.,  
1232 Sherry, C., Jacob, D. J., Jeong, S., Irving, B., and Weitz, M.: A Gridded Inventory of Annual 2012–2018 U.S.  
1233 Anthropogenic Methane Emissions, *Environ. Sci. Technol.*, 57, 16276–16288,  
1234 <https://doi.org/10.1021/acs.est.3c05138>, 2023.
- 1235 MacKay, K., Benmergui, J., Williams, J. P., Omara, M., Himmelberger, A., Sargent, M., Warren, J. D., Miller, C. C.,  
1236 Roche, S., Zhang, Z., Franklin, J., Guanter, L., Wofsy, S., and Gautam, R.: Assessment of methane emissions from  
1237 US onshore oil and gas production using MethaneAIR measurements, *Atmospheric Chemistry and Physics*, 26,  
1238 1179–1192, <https://doi.org/10.5194/acp-26-1179-2026>, 2026.
- 1239 Miller, D. J., Sun, K., Tao, L., Pan, D., Zondlo, M. A., Nowak, J. B., Liu, Z., Diskin, G., Sachse, G., Beyersdorf, A.,  
1240 Ferrare, R., and Scarino, A. J.: Ammonia and methane dairy emission plumes in the San Joaquin Valley of California  
1241 from individual feedlot to regional scales, *Journal of Geophysical Research: Atmospheres*, 120, 9718–9738,  
1242 <https://doi.org/10.1002/2015JD023241>, 2015.
- 1243 Neal, R. M.: MCMC using Hamiltonian dynamics, *Handbook of markov chain monte carlo*, 47–95, 2011.
- 1244 Nesser, H., Jacob, D. J., Maasakkers, J. D., Lorente, A., Chen, Z., Lu, X., Shen, L., Qu, Z., Sulprizio, M. P., Winter,  
1245 M., Ma, S., Bloom, A. A., Worden, J. R., Stavins, R. N., and Randles, C. A.: High-resolution US methane emissions

1246 inferred from an inversion of 2019 TROPOMI satellite data: contributions from individual states, urban areas, and  
1247 landfills, *Atmospheric Chemistry and Physics*, 24, 5069–5091, <https://doi.org/10.5194/acp-24-5069-2024>, 2024.

1248 Nisbet, E. G., Fisher, R. E., Lowry, D., France, J. L., Allen, G., Bakkaloglu, S., Broderick, T. J., Cain, M., Coleman,  
1249 M., Fernandez, J., Forster, G., Griffiths, P. T., Iverach, C. P., Kelly, B. F. J., Manning, M. R., Nisbet-Jones, P. B. R.,  
1250 Pyle, J. A., Townsend-Small, A., al-Shalaan, A., Warwick, N., and Zazzeri, G.: Methane Mitigation: Methods to  
1251 Reduce Emissions, on the Path to the Paris Agreement, *Reviews of Geophysics*, 58, e2019RG000675,  
1252 <https://doi.org/10.1029/2019RG000675>, 2020.

1253 Omara, M., Zimmerman, N., Sullivan, M. R., Li, X., Ellis, A., Cesa, R., Subramanian, R., Presto, A. A., and  
1254 Robinson, A. L.: Methane Emissions from Natural Gas Production Sites in the United States: Data Synthesis and  
1255 National Estimate, *Environ. Sci. Technol.*, 52, 12915–12925, <https://doi.org/10.1021/acs.est.8b03535>, 2018.

1256 Omara, M., Zavala-Araiza, D., Lyon, D. R., Hmiel, B., Roberts, K. A., and Hamburg, S. P.: Methane emissions from  
1257 US low production oil and natural gas well sites, *Nat Commun*, 13, 2085, <https://doi.org/10.1038/s41467-022-29709-3>, 2022.

1259 Omara, M., Gautam, R., O'Brien, M. A., Himmelberger, A., Franco, A., Meisenhelder, K., Hauser, G., Lyon, D. R.,  
1260 Chulakadabba, A., Miller, C. C., Franklin, J., Wofsy, S. C., and Hamburg, S. P.: Developing a spatially explicit  
1261 global oil and gas infrastructure database for characterizing methane emission sources at high resolution, *Earth  
1262 System Science Data*, 15, 3761–3790, <https://doi.org/10.5194/essd-15-3761-2023>, 2023.

1263 Omara, M., Himmelberger, A., MacKay, K., Williams, J. P., Benmergui, J., Sargent, M., Wofsy, S. C., and Gautam,  
1264 R.: Constructing a measurement-based spatially explicit inventory of US oil and gas methane emissions (2021),  
1265 *Earth System Science Data*, 16, 3973–3991, <https://doi.org/10.5194/essd-16-3973-2024>, 2024.

1266 Pendergrass, D. C., Jacob, D. J., Balasus, N., Estrada, L., Varon, D. J., East, J. D., He, M., Mooring, T. A., Penn, E.,  
1267 Nesser, H., and Worden, J. R.: Trends and seasonality of 2019–2023 global methane emissions inferred from a  
1268 localized ensemble transform Kalman filter (CHEEREIO v1.3.1) applied to TROPOMI satellite observations,  
1269 *Atmospheric Chemistry and Physics*, 25, 14353–14369, <https://doi.org/10.5194/acp-25-14353-2025>, 2025.

1270 Qu, Z., Jacob, D. J., Shen, L., Lu, X., Zhang, Y., Scarpelli, T. R., Nesser, H., Sulprizio, M. P., Maasakkers, J. D.,  
1271 Bloom, A. A., Worden, J. R., Parker, R. J., and Delgado, A. L.: Global distribution of methane emissions: a  
1272 comparative inverse analysis of observations from the TROPOMI and GOSAT satellite instruments, *Atmospheric  
1273 Chemistry and Physics*, 21, 14159–14175, <https://doi.org/10.5194/acp-21-14159-2021>, 2021.

1274 Robertson, A. M., Edie, R., Field, R. A., Lyon, D., McVay, R., Omara, M., Zavala-Araiza, D., and Murphy, S. M.:  
1275 New Mexico Permian Basin Measured Well Pad Methane Emissions Are a Factor of 5–9 Times Higher Than U.S.  
1276 EPA Estimates, *Environ. Sci. Technol.*, 54, 13926–13934, <https://doi.org/10.1021/acs.est.0c02927>, 2020.

1277 Saunio, M., Martinez, A., Poulter, B., Zhang, Z., Raymond, P. A., Regnier, P., Canadell, J. G., Jackson, R. B., Patra,  
1278 P. K., Bousquet, P., Ciais, P., Dlugokencky, E. J., Lan, X., Allen, G. H., Bastviken, D., Beerling, D. J., Belikov, D.  
1279 A., Blake, D. R., Castaldi, S., Crippa, M., Deemer, B. R., Dennison, F., Etiope, G., Gedney, N., Höglund-Isaksson,  
1280 L., Holgerson, M. A., Hopcroft, P. O., Hugelius, G., Ito, A., Jain, A. K., Janardanan, R., Johnson, M. S., Kleinen, T.,  
1281 Krummel, P. B., Lauerwald, R., Li, T., Liu, X., McDonald, K. C., Melton, J. R., Mühle, J., Müller, J., Murguía-  
1282 Flores, F., Niwa, Y., Noce, S., Pan, S., Parker, R. J., Peng, C., Ramonet, M., Riley, W. J., Rocher-Ros, G.,  
1283 Rosentretre, J. A., Sasakawa, M., Segers, A., Smith, S. J., Stanley, E. H., Thanwerdas, J., Tian, H., Tsuruta, A.,  
1284 Tubiello, F. N., Weber, T. S., van der Werf, G. R., Worthy, D. E. J., Xi, Y., Yoshida, Y., Zhang, W., Zheng, B., Zhu,  
1285 Q., Zhu, Q., and Zhuang, Q.: Global Methane Budget 2000–2020, *Earth System Science Data*, 17, 1873–1958,  
1286 <https://doi.org/10.5194/essd-17-1873-2025>, 2025.

1287 Scanlon, B. R., Reedy, R. C., Male, F., and Walsh, M.: Water Issues Related to Transitioning from Conventional to  
1288 Unconventional Oil Production in the Permian Basin, *Environ. Sci. Technol.*, 51, 10903–10912,  
1289 <https://doi.org/10.1021/acs.est.7b02185>, 2017.

- 1290 Scarpelli, T. R., Jacob, D. J., Grossman, S., Lu, X., Qu, Z., Sulprizio, M. P., Zhang, Y., Reuland, F., Gordon, D., and  
1291 Worden, J. R.: Updated Global Fuel Exploitation Inventory (GFEI) for methane emissions from the oil, gas, and coal  
1292 sectors: evaluation with inversions of atmospheric methane observations, *Atmospheric Chemistry and Physics*, 22,  
1293 3235–3249, <https://doi.org/10.5194/acp-22-3235-2022>, 2022.
- 1294 Schuit, B. J., Maasakkers, J. D., Bijl, P., Mahapatra, G., van den Berg, A.-W., Pandey, S., Lorente, A., Borsdorff, T.,  
1295 Houweling, S., Varon, D. J., McKeever, J., Jervis, D., Girard, M., Irakulis-Loitxate, I., Gorroño, J., Guanter, L.,  
1296 Cusworth, D. H., and Aben, I.: Automated detection and monitoring of methane super-emitters using satellite data,  
1297 *Atmospheric Chemistry and Physics*, 23, 9071–9098, <https://doi.org/10.5194/acp-23-9071-2023>, 2023.
- 1298 Seymour, S., Xie, D., Kang, M., Schwietzke, S., Zavala-Araiza, D., and Hamburg, S.: Methane emission intensity  
1299 metrics: unmasking the trade-offs, 2025.
- 1300 Shen, L., Gautam, R., Omara, M., Zavala-Araiza, D., Maasakkers, J. D., Scarpelli, T. R., Lorente, A., Lyon, D.,  
1301 Sheng, J., Varon, D. J., Nesser, H., Qu, Z., Lu, X., Sulprizio, M. P., Hamburg, S. P., and Jacob, D. J.: Satellite  
1302 quantification of oil and natural gas methane emissions in the US and Canada including contributions from  
1303 individual basins, *Atmospheric Chemistry and Physics*, 22, 11203–11215, [https://doi.org/10.5194/acp-22-11203-](https://doi.org/10.5194/acp-22-11203-2022)  
1304 2022, 2022.
- 1305 Shen, L., Jacob, D. J., Gautam, R., Omara, M., Scarpelli, T. R., Lorente, A., Zavala-Araiza, D., Lu, X., Chen, Z., and  
1306 Lin, J.: National quantifications of methane emissions from fuel exploitation using high resolution inversions of  
1307 satellite observations, *Nat Commun.*, 14, 4948, <https://doi.org/10.1038/s41467-023-40671-6>, 2023.
- 1308 Sherwin, E. D., Rutherford, J. S., Zhang, Z., Chen, Y., Wetherley, E. B., Yakovlev, P. V., Berman, E. S. F., Jones, B.  
1309 B., Cusworth, D. H., Thorpe, A. K., Ayasse, A. K., Duren, R. M., and Brandt, A. R.: US oil and gas system  
1310 emissions from nearly one million aerial site measurements, *Nature*, 627, 328–334, [https://doi.org/10.1038/s41586-](https://doi.org/10.1038/s41586-024-07117-5)  
1311 024-07117-5, 2024.
- 1312 Varon, D. J., Jervis, D., McKeever, J., Spence, I., Gains, D., and Jacob, D. J.: High-frequency monitoring of  
1313 anomalous methane point sources with multispectral Sentinel-2 satellite observations, *Atmospheric Measurement*  
1314 *Techniques*, 14, 2771–2785, <https://doi.org/10.5194/amt-14-2771-2021>, 2021.
- 1315 Varon, D. J., Jacob, D. J., Hmiel, B., Gautam, R., Lyon, D. R., Omara, M., Sulprizio, M., Shen, L., Pendergrass, D.,  
1316 Nesser, H., Qu, Z., Barkley, Z. R., Miles, N. L., Richardson, S. J., Davis, K. J., Pandey, S., Lu, X., Lorente, A.,  
1317 Borsdorff, T., Maasakkers, J. D., and Aben, I.: Continuous weekly monitoring of methane emissions from the  
1318 Permian Basin by inversion of TROPOMI satellite observations, *Atmospheric Chemistry and Physics*, 23, 7503–  
1319 7520, <https://doi.org/10.5194/acp-23-7503-2023>, 2023.
- 1320 Varon, D. J., Jacob, D. J., Estrada, L. A., Balasus, N., East, J., Pendergrass, D. C., Chen, Z., Sulprizio, M. P., Omara,  
1321 M., Gautam, R., Barkley, Z. R., Cardoso-Saldaña, F. J., Reidy, E. K., Kamdar, H., Sherwin, E. D., Biraud, S., Jervis,  
1322 D., Pandey, S., Worden, J., Bowman, K. W., Maasakkers, J. D., and Kleinberg, R. L.: Seasonality and declining  
1323 intensity of methane emissions from the Permian and nearby US oil and gas basins, 2025.
- 1324 Vecchi, N. T., Mellqvist, J., Samuelsson, J., Offerle, B., and Scheutz, C.: Ammonia and methane emissions from dairy  
1325 concentrated animal feeding operations in California, using mobile optical remote sensing, *Atmospheric*  
1326 *Environment*, 293, 119448, <https://doi.org/10.1016/j.atmosenv.2022.119448>, 2023.
- 1327 Veefkind, J. P., Aben, I., McMullan, K., Förster, H., de Vries, J., Otter, G., Claas, J., Eskes, H. J., de Haan, J. F.,  
1328 Kleipool, Q., van Weele, M., Hasekamp, O., Hoogeveen, R., Landgraf, J., Snel, R., Tol, P., Ingmann, P., Voors, R.,  
1329 Kruizinga, B., Vink, R., Visser, H., and Levelt, P. F.: TROPOMI on the ESA Sentinel-5 Precursor: A GMES mission  
1330 for global observations of the atmospheric composition for climate, air quality and ozone layer applications, *Remote*  
1331 *Sensing of Environment*, 120, 70–83, <https://doi.org/10.1016/j.rse.2011.09.027>, 2012.
- 1332 Veefkind, J. P., Serrano-Calvo, R., de Gouw, J., Dix, B., Schneising, O., Buchwitz, M., Barré, J., van der A, R. J.,  
1333 Liu, M., and Levelt, P. F.: Widespread Frequent Methane Emissions From the Oil and Gas Industry in the Permian

- 1334 Basin, *Journal of Geophysical Research: Atmospheres*, 128, e2022JD037479,  
1335 <https://doi.org/10.1029/2022JD037479>, 2023.
- 1336 Warren, J. D., Sargent, M., Williams, J. P., Omara, M., Miller, C. C., Roche, S., MacKay, K., Manninen, E.,  
1337 Chulakadabba, A., Himmelberger, A., Benmergui, J., Zhang, Z., Guanter, L., Wofsy, S., and Gautam, R.: Sectoral  
1338 contributions of high-emitting methane point sources from major US onshore oil and gas producing basins using  
1339 airborne measurements from MethaneAIR, *Atmospheric Chemistry and Physics*, 25, 10661–10675,  
1340 <https://doi.org/10.5194/acp-25-10661-2025>, 2025.
- 1341 Western, L. M., Ramsden, A. E., Ganesan, A. L., Boesch, H., Parker, R. J., Scarpelli, T. R., Tunnicliffe, R. L., and  
1342 Rigby, M.: Estimates of North African Methane Emissions from 2010 to 2017 Using GOSAT Observations, *Environ.*  
1343 *Sci. Technol. Lett.*, 8, 626–632, <https://doi.org/10.1021/acs.estlett.1c00327>, 2021.
- 1344 Worden, J. R., Cusworth, D. H., Qu, Z., Yin, Y., Zhang, Y., Bloom, A. A., Ma, S., Byrne, B. K., Scarpelli, T.,  
1345 Maasackers, J. D., Crisp, D., Duren, R., and Jacob, D. J.: The 2019 methane budget and uncertainties at 1°  
1346 resolution and each country through Bayesian integration Of GOSAT total column methane data and a priori  
1347 inventory estimates, *Atmospheric Chemistry and Physics*, 22, 6811–6841, [https://doi.org/10.5194/acp-22-6811-](https://doi.org/10.5194/acp-22-6811-2022)  
1348 2022, 2022.
- 1349 Yu, J., Hmiel, B., Lyon, D. R., Warren, J., Cusworth, D. H., Duren, R. M., Chen, Y., Murphy, E. C., and Brandt, A.  
1350 R.: Methane Emissions from Natural Gas Gathering Pipelines in the Permian Basin, *Environ. Sci. Technol. Lett.*, 9,  
1351 969–974, <https://doi.org/10.1021/acs.estlett.2c00380>, 2022.
- 1352 Yu, Y., Yin, J., Zheng, J., Li, F., Tao, C., Xu, X., and Wu, H.: Division and resources evaluation of hydrocarbon plays  
1353 in the Amu Darya basin, central Asia, *Petroleum Exploration and Development*, 42, 819–826,  
1354 [https://doi.org/10.1016/S1876-3804\(15\)30078-1](https://doi.org/10.1016/S1876-3804(15)30078-1), 2015.
- 1355